



Hydration of Mafic Crust

Analytical and Numerical Insights

Master Thesis

2023

Jasper Engelmann

Supervisors: Dr. Johannes C. Vrijmoed, Prof. Dr. Timm John

Freie Universität Berlin, Institut für Geologische Wissenschaften

<http://dx.doi.org/10.17169/refubium-40127>

CC BY-NC-SA

Eigenständigkeitserklärung

Hiermit erkläre Ich, dass Ich die vorliegende Arbeit selbstständig verfasst und keine anderen als die angegebenen Quellen und Hilfsmittel verwendet habe. Alle sinngemäß und wörtlich übernommenen Textstellen aus fremden Quellen wurden kenntlich gemacht.

Berlin, den 16.05.2023

Jasper Engelmann

Declaration of Originality

I hereby confirm that the submitted thesis is my own original work and was written without further assistance. Appropriate credit has been given where reference has been made to the work of others.

Berlin, 16.05.2023

Jasper Engelmann

Table of Contents

Abstract	2
Introduction.....	3
Motivation	3
Background and Geological Setting.....	4
Methods	6
Sampling	6
Scanning Electron Microscope (SEM).....	6
Electron Microprobe (EMP).....	7
Data Processing	7
Modeling	8
Results	12
Field Observations	12
Optical and Electron Microscopy	12
Modeling Results	27
Discussion	32
Reactive Fluid Flow Through a Solid Polygranular Medium.....	32
Amphibolitization Mechanisms in the Different Lithologies.....	32
Differences Between the Two Transformations	35
Interpreting the Model Results	36
Conclusion	38
Acknowledgements	39
References.....	39
Supplementary materials	43

Abstract

The grain-scale mechanisms of hydration of mafic lower crustal rocks are investigated through partially amphibolitized samples from the Hustad Igneous Complex in the Western Gneiss Region, Norway. Chemical maps were obtained on continuous rock sections of 20 cm by 2 cm and supplemented with EMP point measurements. Numerical models are employed to reproduce reactive fluid flow driven by a fluid pressure gradient. The Proterozoic pyroxenite body and dolerite dike show different responses to the exposure to hydrous fluids along fractures formed during late Caledonian extension and exhumation. While the dolerite reaches full amphibolitization in a cm-scale reaction halo with a dm-scale transition zone, the pyroxenite has experienced previous metamorphism and is less affected by this event. Dissolution precipitation reactions and slightly faster grain boundary assisted flow are identified as the main mechanisms of fluid flow through the rock and limited element mobility is documented by grain scale chemical gradients in forming amphibole. Phase diagram calculations yield a P/T-window between 650 – 730°C and 0.4 – 0.6 GPa for amphibolite formation. 1D numerical models of reactive fluid flow driven by a fluid pressure gradient show the reaction and reproduce differences in front propagation speed between the two lithologies as observed in the samples. A simple 2D model is employed to demonstrate that the gradual transition from dolerite to amphibolite can be achieved by implementing higher permeability along grain boundaries, supported by the observation that flow along boundaries continues before individual grains are fully replaced.

Introduction

Fluids play a role across Earth's geological domains and cycles, from magmatic processes (e.g., Audétat and Edmonds 2020) to erosion and sedimentation (e.g., Finnie 1995), from alteration below the ocean floor (e.g., Schwarzenbach and Steele-MacInnis 2020) to dehydration of subducting material (e.g., Manning and Frezzotti 2020), from surface weathering (e.g., Maher 2010) to eclogite-facies metamorphism (e.g., Austrheim 1987).

Investigating the impact of fluid flow and interaction with lower crustal rocks presents an interesting window into the physical and chemical processes within our continents. Understanding what happens when aqueous fluids circulate during tectonic events in these areas may give insight into the formation and break-up of continents, the occurrence and frequency of earthquakes (e.g., Reyners et al. 2007), and the element and energy cycles of the Earth system (e.g., Kerrick and Connolly 2001, Manning 2004, Evans et al. 2013, Li et al. 2020), as fluids provide a geologically very fast way of transporting both matter and energy within Earth's outer layers (e.g., Taetz et al. 2018).

Numerical modeling on the basis of local equilibrium thermodynamics is a well-established tool to answer to geological questions. It has proven to be immensely helpful in better understanding the processes deep below the surface of the Earth of which only the results after millions of years can be observed directly. Applications to classical geological research fields are plentiful and include subduction (e.g., Bessat et al. 2020, Candiotti et al. 2022), orogenesis (e.g., Poh et al. 2020, Spitz et al. 2020, Duretz et al. 2021, Vaughan-Hammon et al. 2022), metamorphism and metasomatism (e.g., Schmalholz et al. 2020, Beinlich et al. 2020, Yamato et al. 2022, Huber et al. 2022), or seismic (e.g., Yamato et al. 2022) and volcanic activity (e.g., Rummel et al. 2020, Spang et al. 2022, Kiss et al. 2023), to name just a few recently investigated examples.

Motivation

Introducing hydrous fluids to natural systems below orogens can have a range of effects. Depending on depth, temperature, and fluid and solid composition, water may induce partial melting, facilitate element transport, or influence the rheology (e.g., Evans and Tomkins 2020). Water, or fluids in general, also play an important role in facilitating metamorphism even when no hydrous minerals are involved (e.g., Putnis and John 2010, Plümpner et al. 2012, Zertani et al. 2022, Kaatz et al. 2022). Direct observation of fluid rock interaction at crustal depths is impossible, but paleo-orogens with long histories of exhumation and erosion can bring the products of such processes to the surface, where they can be studied as analogues to contemporary natural systems. To be used as predictive tools, numerical models capable of reproducing the results observed in the rock record need to be developed, based on fundamental physical principles such as energy conservation and non-negative entropy production.

This study aims to investigate the initial stages of lower crustal hydration by developing such a model, focusing on some key questions:

1. What grain-scale mechanisms facilitate the propagation of reactive fluid flow through effectively impermeable rocks at crustal depth? How and why do these mechanisms change in different lithologies exposed to the same conditions?
2. How can a reaction front of a fluid-consuming reaction be supplied with the necessary fluid to continue reactive fluid flow into the rock? How does rock chemistry and mineralogy influence front propagation?

To answer these questions, lower crustal rocks from western Norway are investigated along 20 cm wide cross sections. These rocks record reactive fluid flow under amphibolite-facies conditions during late Caledonian extension along fractures and show a gradient from zero to complete hydration within the cross sections. Thus, they serve as analogue to contemporary processes below orogens, frozen in time. A numerical model with fluid flow based on fluid pressure gradients is developed to reproduce the observed reaction zones.

Background and Geological Setting

Continental Crust

Continental crust is generally divided into 3 layers: the upper, middle, and lower crust (e.g., Rudnick and Gao 2014, Sammon and McDonough 2021), with variable thickness and composition depending on geological history and tectonic setting. While the upper crust is exposed to the surface and much is known about its composition and the processes within it, less certainty exists about the makeup and behavior of the middle and lower sections of the continents. There is a general understanding that continental crust gets more mafic with depth (e.g., Wedepohl 1995, Rudnick and Gao 2014, Sammon and McDonough 2021), and exposed sections such as the Ivrea-Verbano zone in northern Italy suggest ultramafic compositions in the lowermost crust (Berckhemer 1968). On the other hand, the available geophysical data has been shown to be satisfied over a range of lower crustal compositions (Hacker et al. 2015), though still always including a mafic part of the lower crust.

Crustal Fluids

Crustal fluids are composed of mostly water, with other volatiles such as carbon dioxide or sulfur, salts (mainly NaCl) or aqueous silica in variable concentrations (e.g., Evans and Tomkins 2020, Steele-MacInnis and Manning 2020). They can also carry significant amounts of economic metals to facilitate orebody-formation (e.g., Audétat and Edmonds 2020).

Fluids in the deep crust can be sourced from dehydrating subducting slabs by compaction of fluid-filled pores or dehydration reactions (e.g., Zheng et al. 2016, Manning and Frezzotti 2020), as residual fluids from magmatic processes (e.g., Audétat and Edmonds 2020, Park et al. 2021), or on a larger scale by mantle devolatilization (e.g., Pollack 1986, Steele-MacInnis and Manning 2020).

Amphibolitization

The term amphibolitization describes the metamorphic transformation of a usually mafic rock to an amphibolite. First coined by Eskola (1915), the amphibolite facies is loosely defined between 500 – 750°C and 0.2 – 1 GPa, though the transitions between metamorphic assemblages are highly dependent on chemical composition, and these facies were defined for metabasites with limited application to other protoliths.

A typical amphibolite, formed from a mafic composition, will normally consist mainly of amphibole (hornblende) and plagioclase, with garnet appearing in higher pressure amphibolite and chlorite and/or epidote in the lower temperature range (Miyashiro 1973, Bucher 2023). The plagioclase becomes more calcic towards higher grade conditions (e.g., Apter and Liou 1983, Spear 1982, Maruyama et al. 1983).

Prograde amphibolite facies metamorphism is typically associated with continental collision and an intermediate P/T gradient (England and Thompson 1984), while retrograde metamorphism under amphibolite-facies conditions often occurs during exhumation, depending on the availability of fluids (e.g., Hacker et al. 2010).

Hydrous fluid input into the rock is a prerequisite for amphibolitization, so the process is clearly dependent on fluid availability. However, it is worth noting that most metamorphic reactions require the presence of fluids, if only ephemeral in higher grade conditions (e.g., Putnis and John 2010).

Norwegian Geology

The Scandinavian Caledonides provide a great natural laboratory for studying fluid-rock interaction processes within the deep crust (e.g., Austrheim 1987, Beinlich et al. 2020, Kaatz et al. 2021, Zertani et al. 2022). They represent part of a Paleozoic orogen with a mostly Proterozoic basement (Corfu et al. 2014) with great temporal, structural and lithological variety. The Caledonian orogen formed by closure of the Iapetus ocean and subsequent collision of the continents Baltica and Laurentia around 430 million years ago (Cocks and Torsvik 2002, Corfu et al. 2014).

The investigated rocks lie in the Western Gneiss Region (WGR), a large area of reworked Proterozoic basement where most rocks exposed today are orthogneisses, though a number of peridotite lenses, a few igneous complexes and a Devonian sedimentary basin are also part of this region (Hacker et al. 2010, Corfu et al. 2014). Metamorphism is recorded all throughout the area, reaching from the amphibolite facies to UHP conditions (e.g., Vrijmoed et al. 2006, Hacker et al. 2010).

Since deformation on all scales involves areas of high and low strain (e.g., Griera et al. 2011, Boutonnet et al. 2013), it is not surprising that the Western Gneiss Region contains some enclaves that show few to no signs of deformation despite being older than the deformation in the surrounding rocks. This provides the opportunity to investigate samples with little coupling of deformation and reactive fluid flow.

The Hustad Igneous Complex

Initially mentioned in a mapping campaign in the area (Hernes 1955) and described in detail, mapped and dated by Austrheim et al. (2003), the Hustad Igneous Complex (HIC) is located close to the Norwegian city of Molde (Fig. 1). It lies only about 25 km away from UHP rocks (Vrijmoed et al. 2006) and within the region most strongly affected by Scandian deformation (Hacker et al. 2010), recorded by a strong east to west striking gneissic foliation in the rocks around the complex (Hernes 1955).

The main body of the HIC is a 1.6 Ga old, granitic to monzodioritic, calc-alkaline pluton (Fig. 1) that escaped some of the most intense deformation of the Western Gneiss region. Some metamorphism is recorded in the complex, but it is almost devoid of ductile deformation, occurring only on the boundary to the surrounding gneiss. It represents a low strain enclave in the WGR (Austrheim et al. 2003).

Opposite the bay of Breivik lies the Nordneset peninsula, where mafic igneous rocks are exposed, associated to the granitic body (Fig. 1). The main rock on the peninsula is a mafic to ultramafic layered intrusion, referred to as pyroxenite by the authors of the previous study (Austrheim et al. 2003). Both bodies are cut by a ca. 40 m wide dolerite dike, dated to 1.2 Ga.

The entire complex contains later stage extensional fractures, cutting through dolerite dike and pyroxenite, sometimes filled with up to 0.5 m thick quartz pegmatites with Caledonian ages (Austrheim et al. 2003). Amphibolite reaction halos of variable thickness (from a few cm to dm) are present around these fractures, indicating their formation on the retrograde path during exhumation of the region (Hacker et al. 2010).

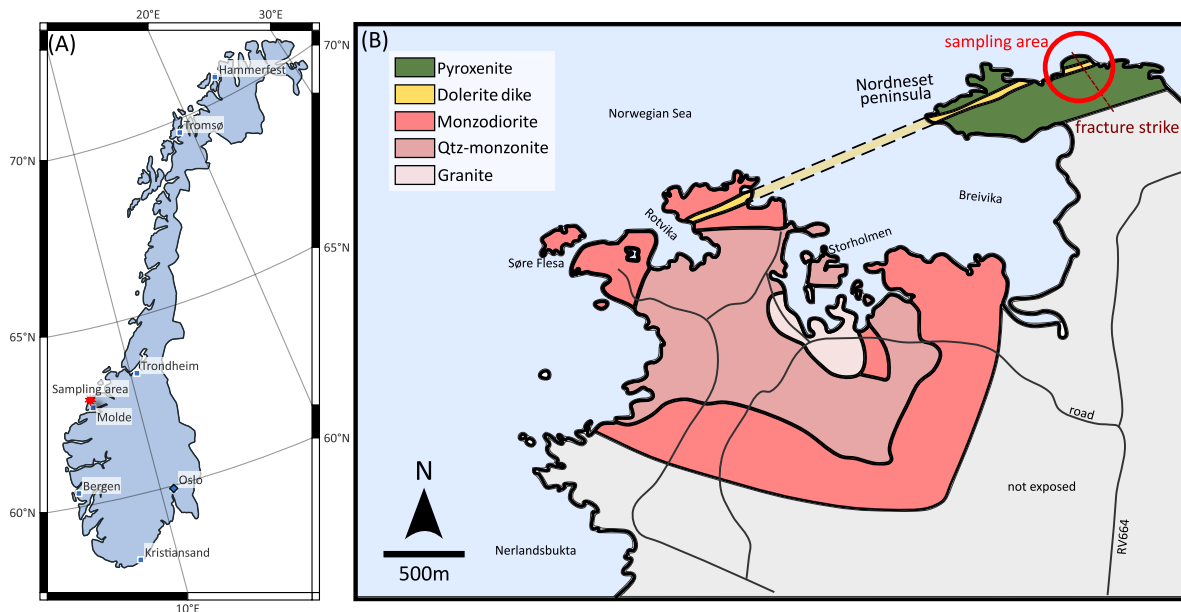


Figure 1: (A) Map of Norway with main cities and location of the sampling area. Created with QGIS. (B) Geological map of the Hustad Igneous Complex (Austheim et al. 2003), with indicated sampling area and strike direction of the observed fractures.

Methods

All measurements and sample preparation took place in the facilities of the Free University Berlin.

Sampling

To investigate the transition from unaffected to fully hydrated rock in the two lithologies present on the Nordneset peninsula, four cross-sections of 20 – 30 cm were cut with a portable electric blade saw. The cuts were made perpendicular to the observed fractures and wide enough to include the entire amphibolite facies reaction halo. Three sections were taken in the dolerite dike and one in the surrounding pyroxenite body. They were all cut and polished into continuous sets of thin sections, and two entire cross-sections were investigated with optical and electron microscopy. The first is from a crack hosted in the dolerite (thin sections HU01 – 05), the second from the pyroxenite (thin sections HU21 – 25). The distance between the two sampling points is about 30 m. While they are not on the same fracture, both structures are parallel and have an about equally thick pegmatite filling (~ 10cm).

Scanning Electron Microscope (SEM)

With the aim to investigate and quantify changes in mineral paragenesis and rock chemistry related to reactive fluid flow initiated at the described fractures, chemical maps of the samples were obtained. Five full thin section maps per sample were taken using the Bruker Quantax Xflash energy dispersive spectroscopy (EDS) detectors installed on a Zeiss Sigma 300VP Field Emission SEM. Ordered by atomic number, the elements mapped and used for interpretation were O, Na, Mg, Al, Si, K, Ca, Ti, Mn, and Fe. Some other elements (F, P, S, Cl, Cr, Ni, Cu, Zn, Zr, and Hf) were also mapped but, as they appeared only in accessory phases or were below the detection limit of the setup, not included in further processing.

The pixel size was set to 40 μm , with a dwell time of 0.01 s. The measurements took place at an acceleration voltage of 20 kV, a working distance of 8.5 mm and an aperture diameter of 120 μm . The maps were obtained and quantified using the Zeiss Mineralogic Software and Bruker Esprit internal standardization methodology. All analyses are normalized to 100 wt% as the only available option in Mineralogic. Quantified maps were further analyzed using MATLAB codes developed in this project.

Electron Microprobe (EMP)

To corroborate and cross-check data processed from the SEM, a JEOL JXA 8200 Superprobe was employed for localized precise chemical analysis on selected phases (amphibole, garnet, pyroxenes), using wavelength-dispersive spectrometry (WDS). Chemical composition was determined in oxide weight percent; SiO₂, TiO₂, Al₂O₃, Cr₂O₃, FeO, MnO, MgO, CaO, Na₂O, and K₂O were measured. A beam current of 20 nA, a beam diameter of 1 μm, and an acceleration voltage of 15 kV were used for the point measurements. The peak measurement time was set to 20 s and the background to 10 s. Na was measured for 10 and 5 s, respectively, to avoid Na migration.

Garnet and the transition from clinopyroxene to amphibole were mapped on the microprobe, investigating chemical zonation in the minerals. For both, maps were taken with a 1 μm pixel size, 120 ms dwell time, 15 kV acceleration voltage and 60 nA beam current.

Data Processing

Aside from the already measured elements and mineral paragenesis, the distribution of H₂O concentration in the affected rock would constrain fluid penetration depth. The applied measurements techniques are not capable of measuring hydrogen, so a post-processing method was developed to calculate the water content of present hydrous phases. The same procedure enables automated creation of mineral maps and pixel-by-pixel endmember compositions based on stoichiometric composition ranges of solid solutions.

All X-Ray maps produced at the SEM were processed into phase pseudo color images by comparing each pixel to a set of possible chemical compositions, calculated using the solution models available in the thermodynamic calculation package Thermolab (Vrijmoed and Podladchikov 2022). The possible minerals were chosen according to polarization microscopy observations. Any hydrogen in the formula of compared phases was removed, as it cannot be measured by the instrument. Subsequently, the idealized dry compositions are normalized to 100 wt% to match the gathered dataset.

Pixels where the total deviation from any ideal composition is exceptionally large (>30 wt%) indicate accessory phases not in the list (such as carbonates, sulfides, apatite). Thus, these data were not considered in further processing. All maps were initially processed at a low resolution of solution models to identify the phase, and then reprocessed with a much higher compositional resolution of only the predetermined phase, reducing computing times and memory requirements. About 500 000 single datapoints were taken on each thin section, each first matched with 722 rough compositions, and refined with ca. 20 000 total mineral compositions. The sheer number of datapoints results in statistical distribution of mineral compositions, matching well with microprobe point analysis for some minerals (garnet, feldspar), but prone to systematic error for some phases caused by microscale intergrowth of, for example, quartz and amphibole.

After the classification, the amount of H₂O in each datapoint can be determined. Where measured composition matches best with the ideal composition of a hydrous phase (amphibole/biotite), the water content of that best fitting ideal composition was added to the measured composition. Doing this for all datapoints where a hydrous phase was identified results in a distribution map of water concentration, analogous to any other quantified oxide concentration map.

To avoid mixed measurements, especially where the abundance and grain size of a phase is exceedingly small, image processing was employed to remove all datapoints from the classification that were connected to fewer than 2 other pixels of the same phase.

This moved the resulting mean phase-composition significantly closer to the EMP point measurements for phases of low abundance and has close to no impact on abundant phases.

Finally, the thin section phase and chemical maps of each sample cross-section were stitched together, and the modal abundances and oxide concentrations averaged to a 1D line, which was further smoothed using a moving average approach.

Modeling

To compare the formation of amphibolite in the two lithologies, one-dimensional reactive fluid flow models were set up, where the two different rocks were exposed to the same conditions: an increase in fluid pressure on one side of the domain, with fluid flow and dynamic porosity throughout the system.

The tip of the propagating reaction front was assumed to always be fully hydrated, and this hydration was assumed to occur instantaneously. Attention is focused on forces driving the reaction front forward and continuously supplying fluid for reaction and further propagation. The very onset of hydration on the molecular level (e.g., Sievert et al. 2005, Heeb et al. 2023) is beyond the scope of the continuum modeling approach employed here.

A fluid pressure gradient was considered the main driving force of reaction front propagation in the model. Gradients in chemical potential and osmotic pressure (e.g., Plümper et al. 2017b) have been found to drive reactive fluid flow, but were regarded as second order processes here and thus left out of the equations.

The equations governing the model and applied assumptions have been employed previously in similar models (Malvoisin et al. 2015, Plümper et al. 2017a, Beinlich et al. 2020, Huber et al. 2022). A summary of their derivation and applied assumptions is given in the following section, with a list of symbols provided in Table 1.

Symbol	Meaning	Abbr.	Mineral
ρ_f/ρ_s	Fluid/solid density	amp	Amphibole
ρ_{tot}	Total density	bt	Biotite
ρ_{im}	Density of immobile species in the solid	grt	Garnet
C_s^{im}	Concentration of immobile species in the solid	ox	Oxide
v_f/v_s	Velocity of fluid/solid	ilm	Ilmenite
φ	Porosity/relative amount of fluid	mgt	Magnetite
P_f	Fluid pressure	plg	Plagioclase
q_{v_f}	Flux of fluid velocity in x direction	px	Pyroxene
q_D	Darcy flux	cpx	Clinopyroxene
Q_{ρ_f}	Source term of fluid mass balance	opx	Orthopyroxene
Q_{v_f}	Source term of fluid momentum balance	qtz	Quartz
η_f/μ	Fluid viscosity		
$G_{f/s}$	Gibbs free energy of fluid/solid		
k_0	Background permeability		
k_r	Kinetic factor from mass balance		
α	A parameter of Q_{ρ_f}		

Table 1: List of mineral abbreviations and notations used in the equations.

Governing Equations

A two-phase system of a solid and a fluid is considered, where φ represents the volume fraction of fluid, equivalent to porosity in a rock, with $(1 - \varphi)$ being the amount of solid. Derivation of the equations used in the model starts with total mass (eq. I) and fluid momentum (eq. II) conservation:

$$\frac{\partial(\rho_s(1 - \varphi) + \rho_f\varphi)}{\partial t} + \frac{\partial(v_s\rho_s(1 - \varphi) + v_f\rho_f\varphi)}{\partial x} = 0 \quad (I)$$

$$\frac{\partial\rho\varphi v_f}{\partial t} + \frac{\partial\rho\varphi v_f v_f}{\partial x} + \frac{\partial q_{v_f}}{\partial x} = Q_{v_f} \quad (II)$$

The fluid momentum flux q_{v_f} and the source term in eq. II Q_{v_f} are derived by consideration of entropy and energy balance, following the second law of thermodynamics that entropy production must be non-negative. The resulting thermodynamically admissible flux and source term can be defined as follows:

$$q_{v_f} = P_f\varphi - \eta_f \frac{\partial v_f}{\partial x} \quad (III)$$

$$Q_{v_f} = -\alpha(v_f - v_s) + P_f \frac{\partial\varphi}{\partial x} \quad (IV)$$

Substituting equations III, IV into eq. II, expanding the q_{v_f} derivative, and simplifying the equation yields:

$$\rho_f\varphi \underbrace{\left(\frac{\partial v_f}{\partial t} + v_f \frac{\partial v_f}{\partial x}\right)}_{\frac{Dv_f}{Dt} = 0} + v_f \underbrace{\left(\frac{\partial\rho_f\varphi}{\partial t} + \frac{\partial v_f\rho_f\varphi}{\partial x}\right)}_{Q_{\rho_f}} - \underbrace{\frac{\partial\eta_f}{\partial x} \frac{\partial v_f}{\partial x}}_0 + \varphi \frac{\partial P_f}{\partial x} = -\alpha(v_f - v_s) \quad (V)$$

In eq. V, a few things can be recognized and removed with assumptions:

1. The material derivative of fluid velocity $\frac{Dv_f}{Dt} = \frac{\partial v_f}{\partial t} + v_f \frac{\partial v_f}{\partial x}$ becomes zero under the assumption of insignificant fluid inertia.
2. The source term of fluid mass balance $Q_{\rho_f} = \frac{\partial\rho_f\varphi}{\partial t} + \frac{\partial v_f\rho_f\varphi}{\partial x}$ can be expressed as $-k_r(G_f - G_s) = -k_r\Delta_G$, where k_r is a kinetic factor and $G_{f/s}$ the Gibbs free energies of solid and fluid. In the limit of infinitely fast reaction, this term can be neglected.
3. The third assumption of negligible viscous fluid deformation leaves only:

$$\varphi \frac{\partial P_f}{\partial x} = -\alpha(v_f - v_s) \quad (VI)$$

Where, by choosing $\alpha = \frac{\mu}{\varphi k_0}$, the equation can be solved for Darcy flux:

$$q_D = -\frac{k_0\varphi^3}{\mu} \frac{\partial P_f}{\partial x} = \varphi(v_f - v_s) \quad (VII)$$

Now, eq. I can be reshaped by adding and subtracting $v_s\rho_f\varphi$ in the spatial derivative, resulting in an expression containing the Darcy flux from eq. VII:

$$\frac{\partial(\rho_s(1 - \varphi) + \rho_f\varphi)}{\partial t} + \frac{\partial\left(v_s\rho_s(1 - \varphi) + \overbrace{\varphi(v_f - v_s)\rho_f}^{q_D} + v_s\rho_f\varphi\right)}{\partial x} = 0 \quad (VIII)$$

Assuming a non-deforming, non-moving solid, the expression simplifies to:

$$\frac{\partial \rho_{tot}}{\partial t} + \frac{\partial q_D \rho_f}{\partial x} = 0 \quad (IX)$$

An equation that describes the evolution of porosity during reactive fluid flow is derived from mass balance of an immobile component in the solid, which is the sum of all components except H₂O in the model:

$$\frac{\partial \rho_s(1 - \varphi)C_s^{im}}{\partial t} + \frac{\partial \rho_s(1 - \varphi)C_s^{im}v_s}{\partial x} = 0 \quad (X)$$

Where the second term can be disregarded under the previous assumption that the solid does not move or deform ($v_s = 0$). Applying a time integral to the remaining terms and solving for φ gives an analytical solution for porosity:

$$\int_0^t \frac{\partial \rho_s(1 - \varphi)C_s^{im}}{\partial t} dt = \rho_s(t)(1 - \varphi(t))C_s^{im}(t) - \rho_s^0(1 - \varphi_0)C_s^{0,im} = 0 \quad (XI)$$

$$\varphi(t) = 1 - \frac{\rho_s^0(1 - \varphi_0)C_s^{0,im}}{\rho_s(t)C_s^{im}(t)} \quad (XII)$$

The resulting system of equations X and XII now contains 7 unknowns: solid and fluid density (ρ_s, ρ_f), fluid pressure P_f , porosity φ , concentration of immobile components C_s^{im} , initial porosity φ_0 , background permeability k_0 , and dynamic fluid viscosity μ , the latter three of which are considered constant.

Pseudosections and Lookup Tables

To close the system of equations, thermodynamic relations between the variables are employed. The measured bulk compositions, including calculated water content, are entered into Thermolab (Vrijmoed and Podladchikov 2022), and pseudosections over a suitable P/T range are calculated for the rocks, with and without excess fluid. Gibbs energy minimization is performed in a system of ten components: SiO₂, TiO₂, Al₂O₃, FeO, MgO, CaO, Na₂O, K₂O, and H₂O. Slightly simplified solution models from the internally consistent dataset of Holland and Powell (2011) are used in the calculation. MnO is excluded from the calculation. In the dataset, it only appears in solution models of phases that are not observed in the rock (chlorite, chloritoid, staurolite), so any Mn in the system simply results in a tiny presence of either of these phases throughout the P/T-space.

The calculations were done for the parts of the two lithologies where the reaction progressed furthest, to find a P/T-window which explains both parageneses, indicated by the smallest difference to the measured mineral modal abundance.

The determined window of conditions was subsequently used to calculate mineral modal abundances, solid density, and element concentrations, as well as the density of the fluid (pure water) at constant temperature (720°C) over variable pressure (0.5 – 0.7 GPa). The combined concentration of all components except H₂O within the stable solid phases was taken as immobile solid concentration C_s^{im} . From there, lookup tables for linear interpolation of ρ_s, ρ_f and C_s^{im} from fluid pressure were generated. Initial porosity φ_0 was assumed to be on the order of 10^{-3} .

This results in a closed system of equations with two unknowns (P_f , φ) and two equations:

$$\frac{\partial \rho_{tot}}{\partial t} = - \frac{\partial \left(-\frac{k_0 \varphi^3}{\mu} \frac{\partial P_f}{\partial x} \rho_f \right)}{\partial x} \quad (\text{XIII})$$

$$\varphi = 1 - \frac{\rho_s^0 (1 - \varphi_0) C_s^{0,im}}{\rho_s C_s^{im}} \quad (\text{XIV})$$

Model Setup

A 1D domain of 200 equidistant points was set up, with equal $P_f = 0.58 \text{ GPa}$ and $\varphi_0 = 10^{-3}$. All other values were interpolated from the lookup tables or constant. Initial values of ρ_s and C_s^{im} were saved to be used in eq. XIV. To simulate the instantaneous opening of a fracture on the left side of the domain, P_f was set to 0.6 GPa at the boundary, resulting in a fluid pressure gradient. Now, the equations are solved iteratively using a simple pseudotransient approach (e.g., Räss et al. 2019) until mass conservation is achieved before proceeding to the next timestep.

After each timestep, mineral modal abundances are interpolated from the lookup tables to provide an image that can be compared to observations.

Results

Field Observations

The two lithologies described by Austrheim et al. (2003) are clearly discernible in the field. The 40 m wide fine grained (~1 – 5 mm) dolerite dike, crossing the peninsula from SW to NE (Fig. 1B), is made of 40% greyish white feldspar, 20% red garnet, 20% black to dark green pyroxenes, 10% biotite and 5% opaque phases. The pyroxenite body is coarser grained (5 – 10 mm) and mostly dark green, with spots of white plagioclase, red garnet, and occasional quartz. Plagioclase and garnet appear together and in varying abundance, indicating magmatic layering in the body (Austrheim et al. 2003).

Almost perpendicular to the dike (dip direction ~235°), steeply dipping (60 – 80°) extensional fractures cross through both lithologies, most of them filled with up to 0.5 m wide pegmatites. The pegmatites consist mostly of quartz, with some feldspar and occasional carbonates. Both lithologies contain dark amphibolite halos around these fractures, though they are much more pronounced in the dolerite dike, where they reach about 10 – 20 cm into the rock. Along some of the fractures, secondary reaction rims of about 1 cm are visible in light brown. This rim is included in one of the cut sections but absent in the others. As it is likely a later, low-grade overprint, a sample without this rim was chosen for further analysis of the amphibolite facies overprint. The halos in the pyroxenite are harder to see as the color gradient is much weaker and are only a few cm wide in the cut section.

While small shear zones with reaction halos exist in the area, fractures with no observable deformation aside from the fracture itself were chosen for investigation. Fluid rock interaction and deformation are often coupled in nature, but because the focus here lies on the fluid rock interaction, samples without signs of strong deformation are sought out to avoid these coupling effects.

Optical and Electron Microscopy

Dolerite Dike

A scan of the polished whole sample, the generated phase maps and averaged 1D-profiles of phase modal abundance and normalized main element concentration are presented in Figure 2. Densities, mineral abundances, and bulk composition of the thin section are listed in Table 2.

As observed in the field, the samples present an increasing degree of amphibolitization towards the fractures. The main assemblage of the dolerite changes from 40% plagioclase + 20% garnet + 20% clinopyroxene to 43% plagioclase + 39% amphibole + 3% quartz in the amphibolite (Tab. 2). Both assemblages are accompanied by biotite (5 – 10%) and oxides (5 – 10%), revealed to be mainly magnetite and ilmenite through electron microscopy. As these oxides mostly appear intergrown and exsolving from one another, they are treated as one phase in the diagrams and phase maps. Orthopyroxene is present in < 2 vol% in the least affected dolerite, and is absent in the amphibolite. Accessory phases present throughout the sample are apatite, zircon and pyrite.

About 4 cm of the cross-section, corresponding to the first thin section, are completely transformed into amphibolite, with only rare remnants of clinopyroxene cores encased in amphibole. There is a further 8 cm of transition between the two rock types, where replacement of clinopyroxene and garnet by amphibole is incomplete (Fig. 2 A - C). The overall texture and grain size is homogeneous over the sample and no brittle or ductile deformation is observed.

Bulk rock composition, smoothed with the same rolling average as the phase modes and normalized to the mean composition of the sample furthest from the fracture (Fig. 2 D) or calculated as average of each thin section (Tab. 2), indicates that the main chemical change is an input of water. Total Na₂O, K₂O and TiO₂ content all go down slightly and other components (CaO, MgO, FeO) fluctuate locally, but no trend is as clear as the increase in water, almost doubling in the process. The small dip in water content close to the fracture is presumably due to the local absence of biotite (Fig. 2 C, D). Mineral and bulk densities (Tab. 2) indicate a decrease in density from protolith (HU05) to amphibolite (HU01) of ca. 7%, mainly due to the replacement of high-density garnet.

Table 2: Overview of mineral abundances, densities, and bulk compositions for the five thin sections made from the dolerite. Densities in g/cm³ at 720°C, 0.6 GPa, calculated with Thermolab. HU01 is most strongly amphibolitized, HU05 represents the protolith. *Density calculated from EMP data and assumed constant over sample. Other values are calculated from averages of SEM data for each thin section.

	HU01		HU02		HU03		HU04		HU05	
	ρ	vol%								
qtz	2.57	3.50	2.57	1.88	2.57	0.17	–	0	–	0
plg	2.65	43.34	2.64	45.03	2.63	40.24	2.62	41.93	2.61	40.68
grt*	3.93	1.10	3.93	7.92	3.93	15.83	3.93	19.74	3.93	20.19
cpx*	3.33	0.51	3.33	4.25	3.33	18.75	3.33	19.49	3.33	20.37
opx*	3.50	0.49	3.50	0.31	3.50	1.12	3.50	1.88	3.50	1.55
amp*	3.13	39.32	3.13	27.02	3.13	12.83	3.13	3.18	3.13	2.22
bt	2.93	7.05	2.94	9.56	2.95	7.80	2.95	10.64	2.95	11.39
ilm	4.73	2.29	4.74	2.61	4.73	2.64	4.73	2.57	4.73	3.05
mgt	5.08	2.40	5.08	1.41	5.08	0.63	5.08	0.56	5.08	0.54
ρ_{tot}	2.98		3.02		3.13		3.15		3.17	
Bulk composition (wt%)										
SiO ₂	50.64		50.74		50.47		50.34		50.16	
TiO ₂	1.55		1.69		1.74		1.86		2.12	
Al ₂ O ₃	17.39		17.72		16.69		17.27		17.13	
FeO ^{tot}	12.82		12.41		12.85		13.25		13.39	
MgO	5.75		5.30		5.58		5.25		5.24	
CaO	7.59		7.48		8.36		7.19		7.06	
Na ₂ O	2.38		2.66		2.74		3.10		3.15	
K ₂ O	0.73		1.00		0.89		1.16		1.21	
H ₂ O ^{calc}	1.15		1.01		0.67		0.57		0.55	

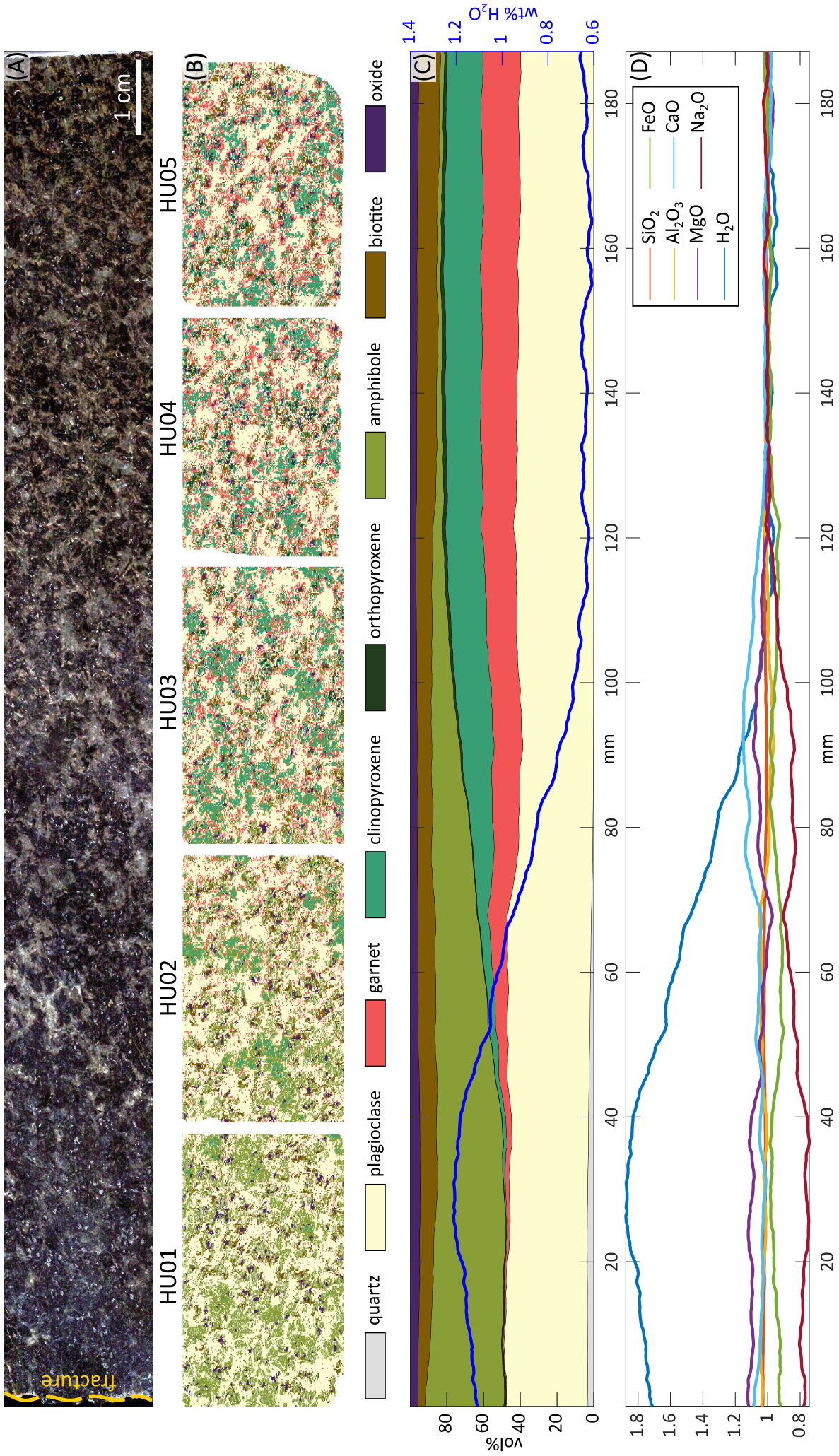


Figure 2: Overview of measurement results for the cross-section from the dolerite dike. (A) Polished hand sample with transition from amphibolite (left) to garnet-bearing dolerite (right). (B) Phase maps of five thin sections cut from the sample, phase names indicated in legend below. (C) 1D average modal mineral abundance over the five thin sections, with calculated water content in the rock. (D) Relative concentration of main components over the five sections, normalized to average HU05 composition.

Pyroxenes

In the rock that is furthest from the fracture and thus least affected by amphibolitization, there are two distinguishable generations of clinopyroxene, about equal in abundance (~10 vol% each). There is some minor orthopyroxene, which only appears in the core of secondary clinopyroxene (Fig. 3).

Primary clinopyroxene (cpx_1) has a dark green to blue color and is full of microscopic ilmenite inclusions, almost appearing opaque in thin section (Fig. 3A). Some grains contain parallel orthopyroxene exsolution lamellae (Fig. 3C). Secondary clinopyroxene (cpx_2) replaces primary orthopyroxene, recording metamorphism in the dike before amphibolite halo formation, possibly related to the Caledonian HP event. It appears light green under polarized light and is fragmented, lacking any planar structures or inclusions (Fig. 3B, D). Occasionally, a core of orthopyroxene appears surrounded by cpx_2 where replacement is incomplete (Fig. 3B). EMP measurements are plotted on the ternary wollastonite-enstatite-ferrosilite diagram in Figure 11A, example measurements are listed in Table 4.

Both clinopyroxenes are diopsitic in composition, and cpx_2 has slightly more Fe and less Mg and Ca, inherited from the orthopyroxene it replaces. Compositionally, orthopyroxene is ca. 55% enstatite and 45% ferrosilite.

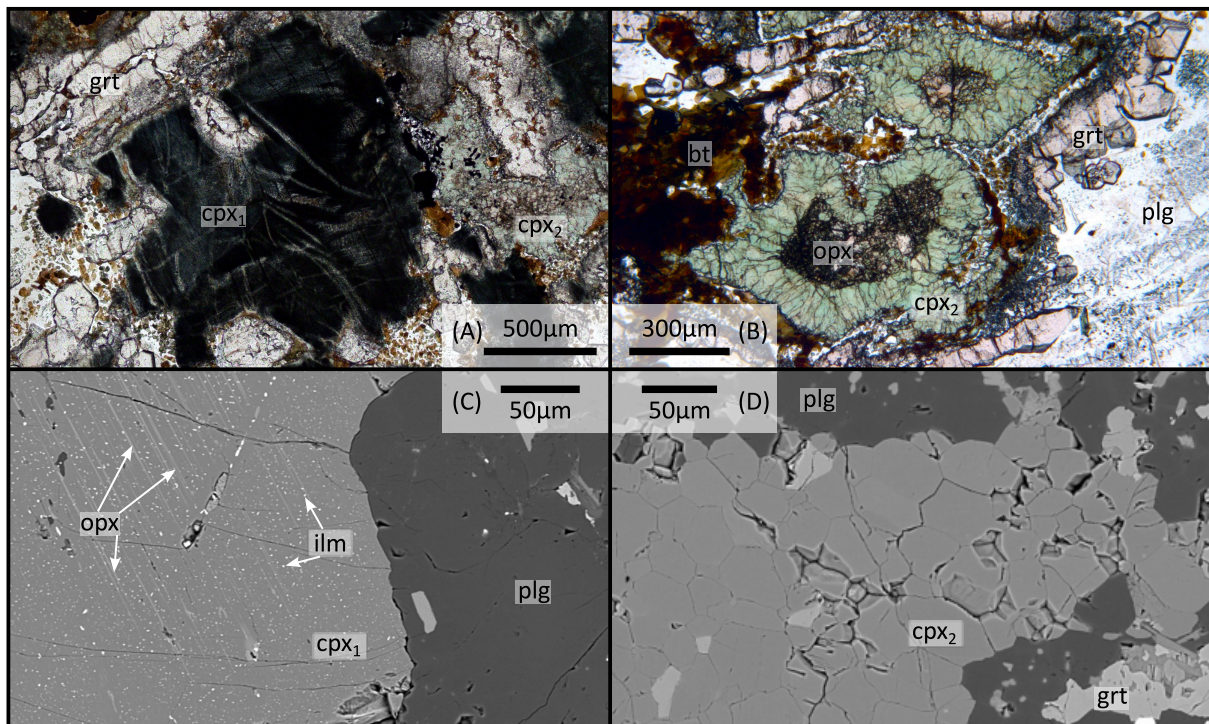


Figure 3: (A) Polarized light image of cpx_1 , with adjacent tabular garnet and cpx_2 . (B) Fragmented cpx_2 with orthopyroxene core, surrounded by garnet and biotite. (C) BSE image of cpx_1 in plagioclase, showing parallel orthopyroxene exsolution lamellae and dotted ilmenite inclusions. (D) BSE image of fragmented cpx_2 in plagioclase. All on thin section HU04.

Amphibole

Within the amphibolite reaction zone, both clinopyroxenes are replaced by blueish-green amphibole from the grain boundary inward, often preserving the cleavage where cpx_1 is replaced (Fig. 4A). Cpx_2 is fully replaced in areas where there are still cores of cpx_1 with amphibole rims. Orthopyroxene is fully replaced in the final assemblage. The gradual increase in amphibole abundance up to about 40 vol% visible in Figure 2C represents the average reactional progress on the grain scale until clinopyroxene is completely replaced.

Replacement in the core of both generations of clinopyroxene often results in a symplectitic intergrowth of amphibole (magnesiohornblende) and quartz, while only amphibole (tschermakite to pargasite) forms at the former grain boundary (Fig. 4, 5, 6, Tab. 3). The symplectite appears in fully replaced grains (Fig. 4A – C), but also in only partially reacted areas (Fig. 6). On some grains, idiomorphic amphibole needles form perpendicular to the grain boundary (Fig. 4D).

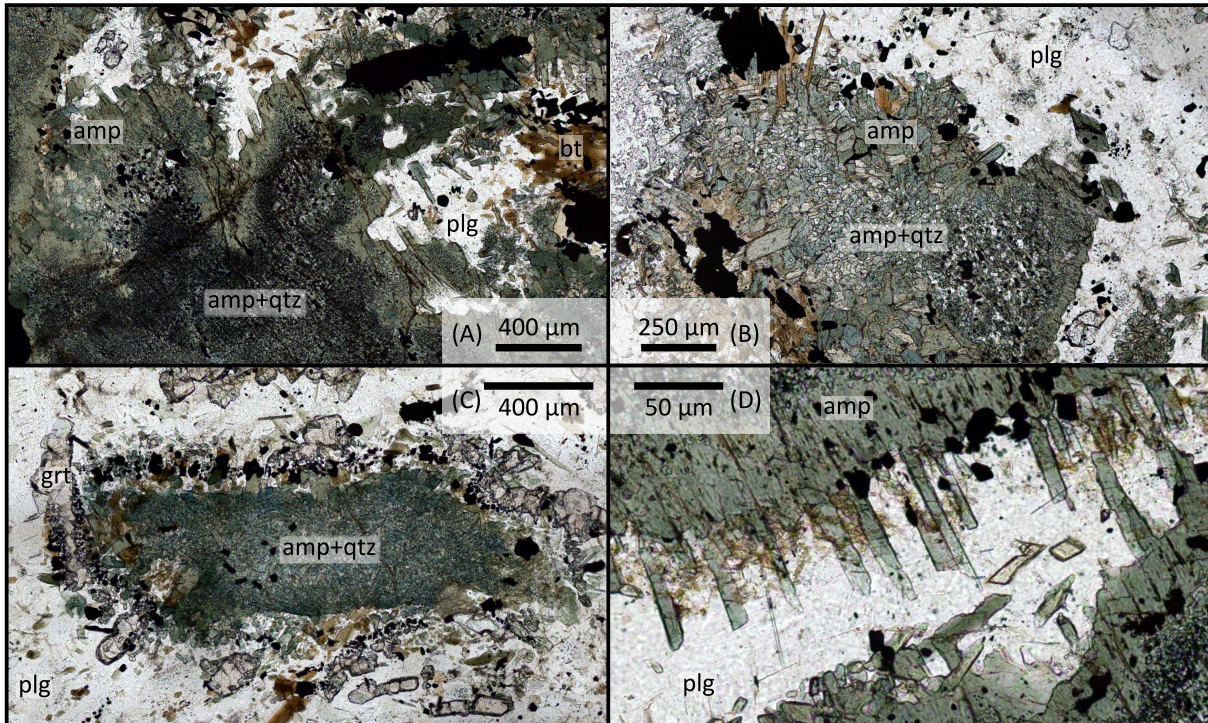


Figure 4: Polarization microscope images of amphibole replacing clinopyroxene. (A) Replacement of cpx_1 , preserving interior structure of the grain. (B) Replacement of cpx_2 and symplectitic intergrowth of amphibole and quartz. (C) Replacement of cpx_2 with partially consumed garnet. (D) Amphibole needles growing on grain boundary. Thin section HU01 (A, B, D) and HU02 (C).

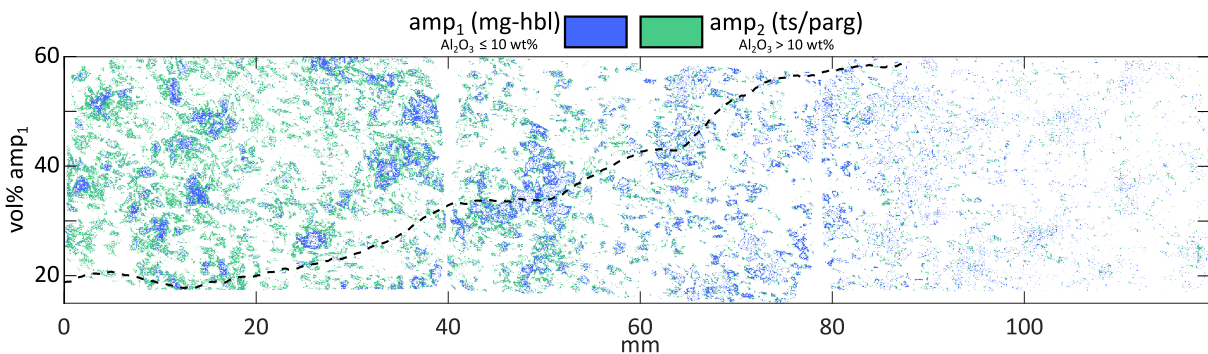


Figure 5: 2D-map of thin sections HU01 – 03 amphibole abundance, split by Al_2O_3 -content to indicate the compositional gradient from magnesiohornblende (core) to tschermakite/pargasite (rim). Dashed line: 1D smoothed average indicating relative amount of low Al-amphibole (i.e. magnesiohornblende), which appears to be the first to form where reaction has just started.

There is a compositional gradient in amphibole on the grain scale from boundary to core, with higher Al, Na, and Fe content on the outside, and more Si and Mg on the inside (Fig. 6). The preserved clinopyroxene core contains more Ca and less Fe than the forming amphiboles, hinting at the involvement of other phases in the reaction. This gradient is reflected in the trend from amp_1 (magnesiohornblende) to amp_2 (tschermakite/pargasite, depending on alkali content) in the classification diagram (Fig. 7) (Leake et al. 1997) for EMP measurements. Dividing all points classified as amphibole on the first three SEM phase maps into two groups at a threshold of 10 wt% Al_2O_3 shows

that amp₁ with low Al, high Si forms at the first contact of pyroxene and water. The farther the reaction has proceeded, the more amp₂ forms on the grain boundaries (Fig. 5), incorporating elements from dissolving garnet and recrystallizing plagioclase.

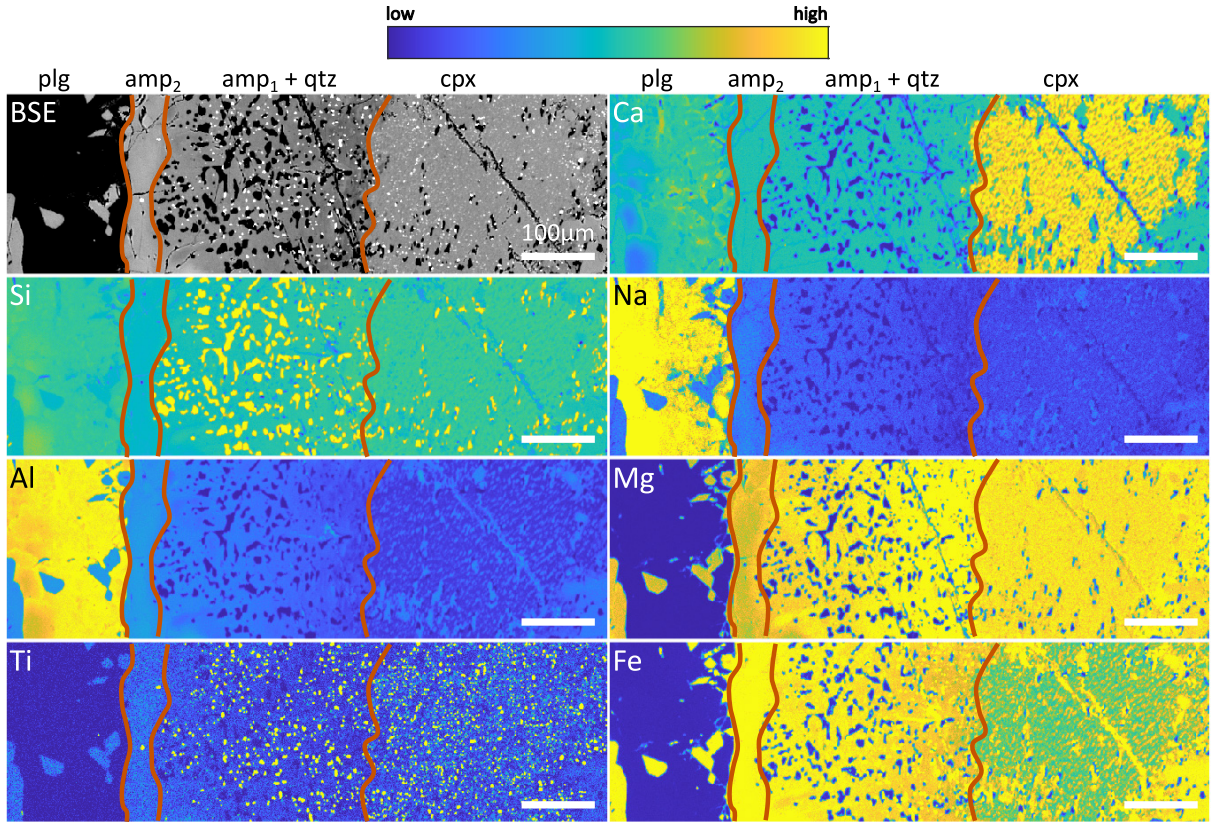


Figure 6: EMP relative concentration maps of clinopyroxene replacement with residual clinopyroxene core, transition zone with amphibole (hornblende) and quartz symplectite and pure amphibole (tschermakite, pargasite) rim. Element gradients of Na, Al, Mg and Fe are very pronounced in the transition zone, also reflected in the BSE image. Ca and Na map additionally show gradients in plagioclase toward the grain boundary. Thin section HU01.

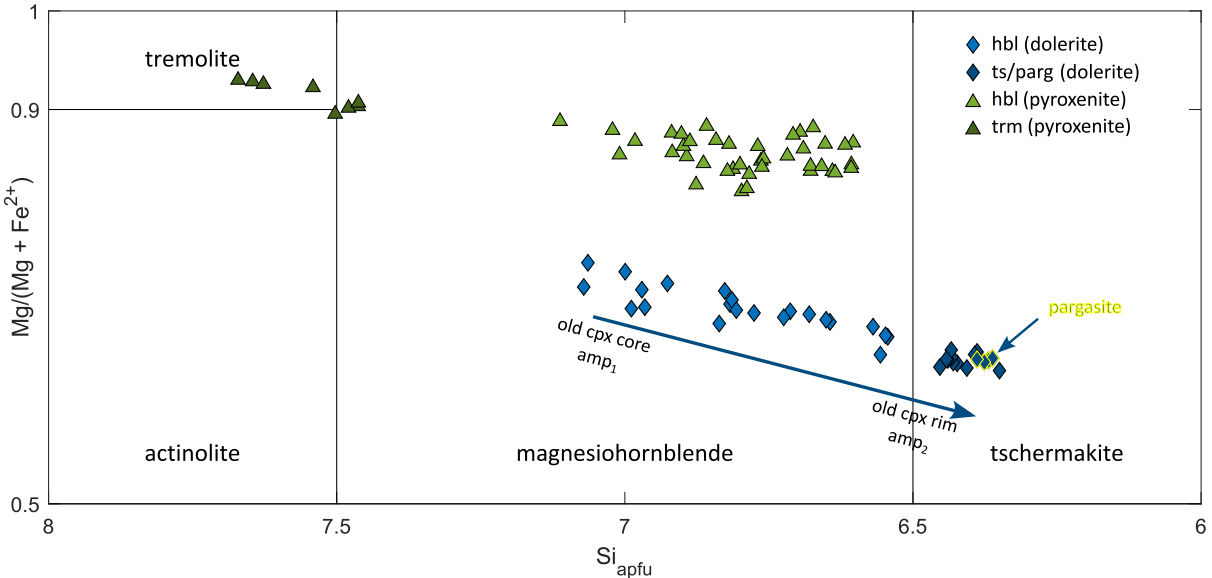


Figure 7: Calcic amphibole classification diagram (Leake et al. 1997) for amphiboles in both lithologies. Calculations using AMFORM (Ridolfi et al. 2018), example point measurements listed in Table 3. Full dataset and calculation spreadsheet in supplements.

Table 3: Summary table of representative microprobe data in weight percent and stoichiometric recalculation for amphibole on the two samples. Calculations of Fe₂O₃, H₂O and stoichiometry using AMFORM (Ridolfi et al. 2018). Classification according to the international mineral association (Leake et al. 1997) as magnesiohornblende (mg-hbl), tschermakite (ts), pargasite (parg), tremolite (trm), and cummingtonite (cum). Full dataset and calculation spreadsheet in supplements.

	Dolerite			Pyroxenite		
	amp ₁ mg-hbl	amp ₂ ts	amp ₂ parg	Mg-hbl	trm	cum
SiO₂	46.61	43.16	43.19	47.91	54.55	56.46
TiO₂	0.64	0.90	0.86	0.41	0.07	0.04
Al₂O₃	9.26	11.92	11.98	9.95	3.43	1.55
Cr₂O₃				0.34	0.19	0.26
FeO^{tot}	13.96	15.59	15.56	7.89	5.20	12.38
MnO	0.20	0.30	0.25	0.10	0.09	0.29
MgO	13.88	11.91	12.20	17.55	21.76	26.48
CaO	12.03	11.83	11.69	11.89	11.99	0.50
Na₂O	0.94	1.26	1.44	1.01	0.31	0.08
K₂O	0.42	0.63	0.66	0.62	0.11	
Totalⁱⁿⁱ	97.94	97.49	97.81	97.67	97.70	98.04
Recalculated values						
Fe₂O₃^{calc}	3.37	3.92	4.08	2.33	2.15	2.45
FeO^{calc}	10.93	12.06	11.89	5.79	3.26	10.18
H₂O^{calc}	1.99	1.84	1.84	2.04	2.17	1.74
Total^{calc}	100.24	99.78	100.05	99.95	100.07	100.01
Stoichiometric calculations based on 23 O						
Si	6.78	6.41	6.39	6.80	7.54	7.81
Al	1.59	2.08	2.09	1.67	0.56	0.25
Ti	0.07	0.10	0.10	0.04	0.01	
Cr				0.04	0.02	0.03
Fe³⁺	0.37	0.44	0.45	0.25	0.22	0.25
Mg	3.01	2.64	2.69	3.71	4.48	5.46
Fe²⁺	1.33	1.50	1.47	0.69	0.38	1.18
Mn	0.02	0.04	0.03	0.01	0.01	0.03
Ca	1.87	1.88	1.85	1.81	1.78	0.07
Na	0.26	0.36	0.41	0.28	0.08	0.02
K	0.08	0.12	0.12	0.11	0.02	
OH	1.94	1.82	1.81	1.93	2.00	1.60
Values used in plotting (Fig. 7)						
Si	6.78	6.41	6.39	6.80	7.54	7.81
Mg/(Mg+Fe)	0.69	0.64	0.65	0.84	0.92	0.82
Na + K	0.34	0.48	0.54	0.39	0.10	0.02

Plagioclase

While plagioclase abundance stays about the same throughout the sample around 40 – 45 vol% (Fig. 2C, Tab. 2), it plays a significant role in the overall reaction: The composition changes from albitic (an_{21}) to anorthitic (an_{45}), where clinopyroxene and garnet are replaced by amphibole. The involvement of plagioclase in the metasomatic reaction is also evident from the microscopic structure, where the previous crystal shape is still recognizable, but recrystallized, anhedral, and small ($<200\ \mu\text{m}$) grains form the new plagioclase, with abundant tiny grains of amphibole and biotite between them (Fig. 8). Locally, the anorthite enrichment occurs close to new forming amphibole (Fig. 6). Over the whole sample and split at 33% anorthite, the change in composition matches well with the first significant occurrence of amphibole (Fig. 9), indicating that excess Ca from dissolving clinopyroxene is moved to the forming plagioclase.

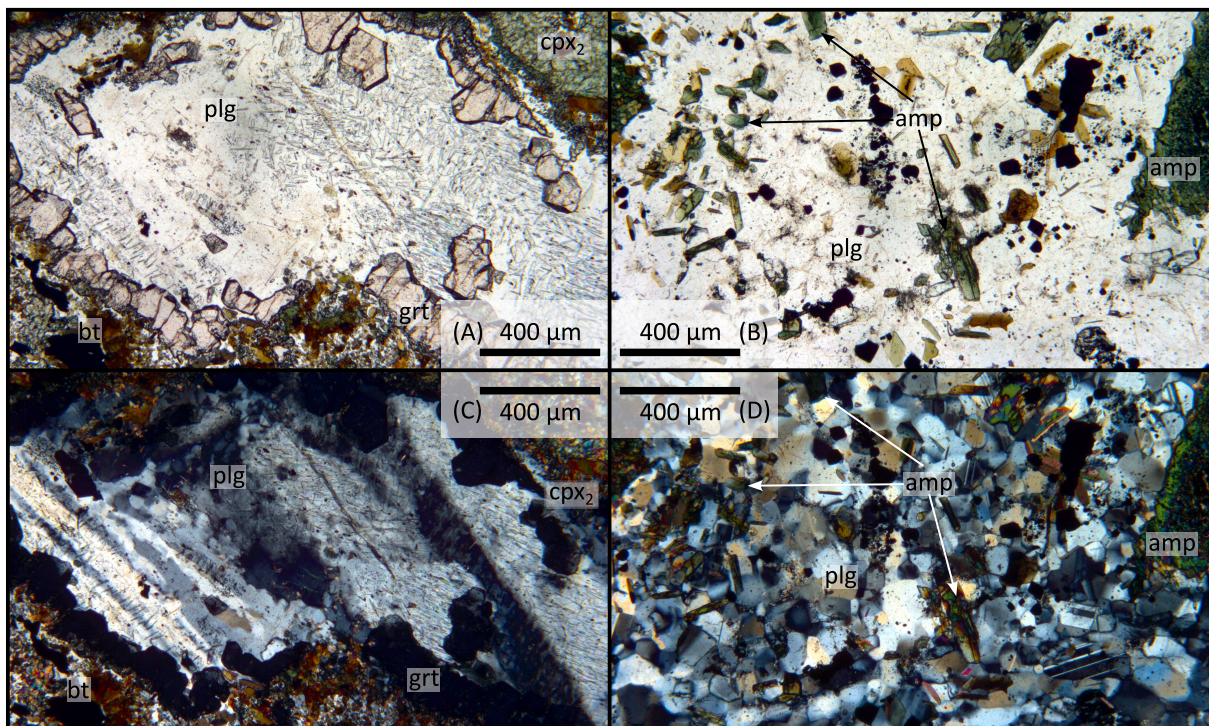


Figure 8: (A) Polarized microscope image of plagioclase in sample HU05, furthest from the fracture, surrounded by secondary garnet and cpx_2 . (B) Secondary plagioclase in sample HU01, close to the fracture and within fully reacted zone, with tiny inclusions of amphibole and biotite. (C) Fig. 8A, under cross-polarized light, showing twinning in plagioclase, grain size ca. $500\ \mu\text{m}$. (D) Fig. 8B, under cross-polarized light, showing small grain size ($<100\ \mu\text{m}$) of secondary plagioclase.

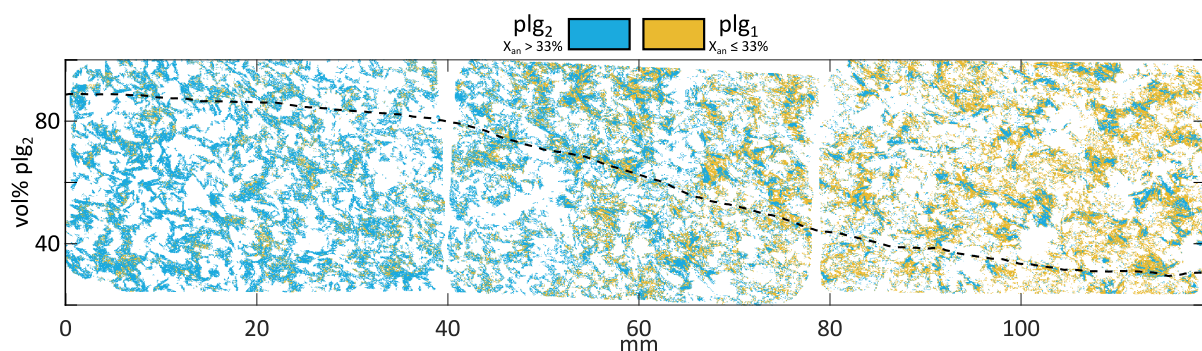


Figure 9: 2D-map of thin sections HU01 – 03 plagioclase abundance, split by X_{an} to indicate the compositional gradient from albitic to anorthitic during amphibolitization. Dashed line: 1D smoothed average indicating relative amount of anorthitic plagioclase (plg_2), which appears coeval with amphibole formation.

Garnet

Garnet often appears in tabular aggregates (Figs. 3A, 3B, 4C, 8A, 8C) in plagioclase or on boundaries between plagioclase and clinopyroxene, replacing primary plagioclase. In the unreacted parts of the rock far from the fracture, garnet constitutes about 20 vol% of the rock (Fig. 2C). Within the reaction zone, garnet disappears almost completely, and is not pseudomorphically replaced but consumed in proximity to forming amphibole. Some grains are not fully dissolved, but show increasingly strong Mn-rims, the closer they are to the fracture, indicated by distance x in Figure 10. These rims are not observed in the unaltered rock, indicating local garnet resorption during amphibolitization, which commonly results in high Mn-rims in garnet (Kohn and Spear 2000). There are two clusters of garnet composition, their main difference being the Ca and resulting grossular + andradite content, observed to be higher in residual garnet close to the fracture (Tab. 4, Fig. 11B).

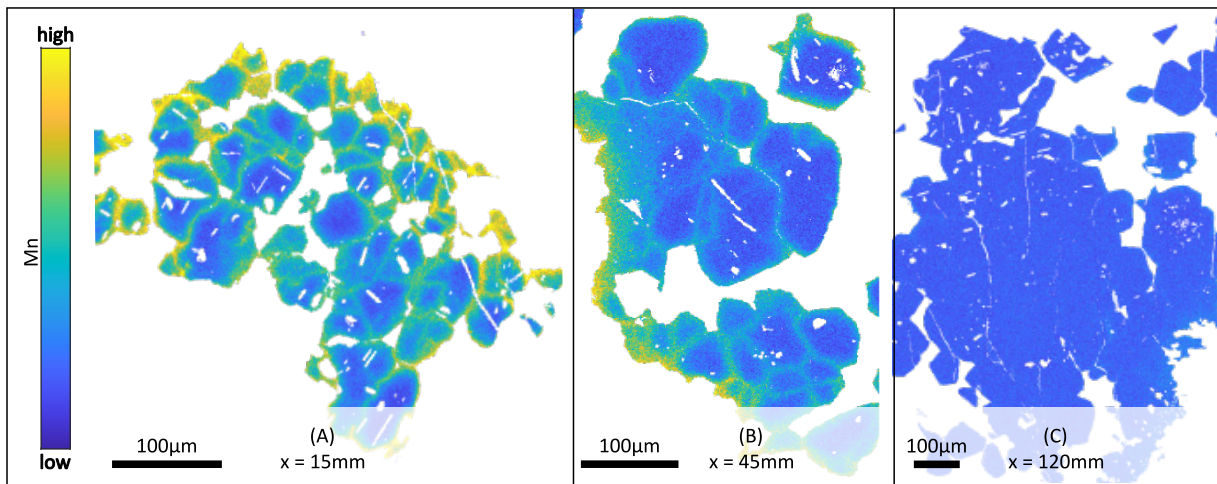


Figure 10: EMP relative concentration Mn maps of garnet in increasing distance to the fracture (left to right, indicated by x). Grains (A) and (B) show that Mn is highest on the sides where garnet is consumed but increased all around the grain.

Table 4: Summary table of representative microprobe data for pyroxenes and garnet on the two samples. Pyroxene Fe_2O_3 is calculated by cation charge balance. Garnet recalculation is done following the methodology by Locock (2008), the endmembers listed are pyrope (prp), almandine (alm), grossular (grs), andradite (adr), and spessartine (sps). Empty spaces indicate results below the detection limit of 0.05 wt%. Full dataset and calculation spreadsheets in supplements.

	Dolerite			Pyroxenite		Dolerite			Pyroxenite		
	cpx ₁	cpx ₂	opx	cpx	opx	grt _{core}	grt _{rim}	grt _{HU05}	grt _{core}	grt _{rim}	
SiO ₂	52.79	52.50	51.89	53.76	54.80	38.72	38.75	38.08	39.85	38.81	
TiO ₂	0.29	0.25	0.09	0.12	0.06	0.01	0.02	0.09	0.05		
Al ₂ O ₃	3.19	4.04	0.95	2.33	1.99	21.13	21.24	21.15	22.55	21.78	
Cr ₂ O ₃				0.13	0.41						
FeO ^{tot}	8.74	10.78	27.20	4.17	13.06	25.06	23.62	27.32	17.24	22.69	
MnO	0.09	0.09	0.23	0.10	0.23	0.68	4.06	0.68	0.82	2.57	
MgO	12.45	10.89	18.98	15.80	29.14	5.22	5.21	5.90	13.07	8.15	
CaO	20.31	18.38	0.37	22.95	0.58	9.14	7.06	6.67	6.30	5.99	
Na ₂ O	2.05	2.65		0.59							
K ₂ O											
Total ⁱⁿⁱ	99.91	99.57	99.70	99.96	100.27	99.98	99.96	99.89	99.85	99.98	
Recalculated values											
Fe ₂ O ₃ ^{calc}	3.50	3.44	0.00	0.54	0.53	0.51	0.00	1.61	2.00	1.19	
FeO ^{calc}	5.60	7.68	27.20	3.84	12.58	24.60	23.62	25.87	15.45	21.62	
Total ^{calc}	100.26	99.91	99.70	99.98	100.29	100.02	99.96	100.05	100.05	100.10	
Stoichiometric calculations based on 6 O											
Si	1.95	1.95	1.98	1.96	1.95						
Ti	0.01	0.01						0.01			
Al	0.14	0.18	0.04	0.10	0.08						
Cr					0.01						
Fe ³⁺	0.10	0.10	0.00	0.01	0.01			0.09	0.11	0.07	
Mg	0.68	0.60	1.08	0.86	1.54			0.69	1.45	0.93	
Fe ²⁺	0.17	0.24	0.87	0.12	0.37			1.69	0.96	1.39	
Mn			0.01		0.01			0.04	0.05	0.17	
Ca	0.80	0.73	0.02	0.90	0.02			0.56	0.50	0.49	
Na	0.15	0.19		0.04							
Based on 12 O											
						3.02	3.03	2.97	2.96	2.98	
						1.94	1.96	1.95	1.97	1.97	
						0.03		0.09	0.11	0.07	
						0.61	0.61	0.69	1.45	0.93	
						1.60	1.54	1.69	0.96	1.39	
						0.04	0.27	0.04	0.05	0.17	
						0.76	0.59	0.56	0.50	0.49	
Values used in plotting (Fig. 11) (all in mol%)											
X _{Wo}	45.68	43.83	0.77	47.62	1.13	X _{prp}	18.20	18.77	22.90	48.21	31.09
X _{En}	38.97	36.12	55.00	45.63	79.01	X _{alm}	53.38	51.49	56.31	31.96	46.28
X _{Fs}	15.35	20.05	44.23	6.76	19.86	X _{grs}	23.88	18.64	15.34	14.61	14.64
						X _{adr}	1.50	–	3.00	2.09	1.77
						X _{sps}	1.50	8.96	1.49	1.73	5.56

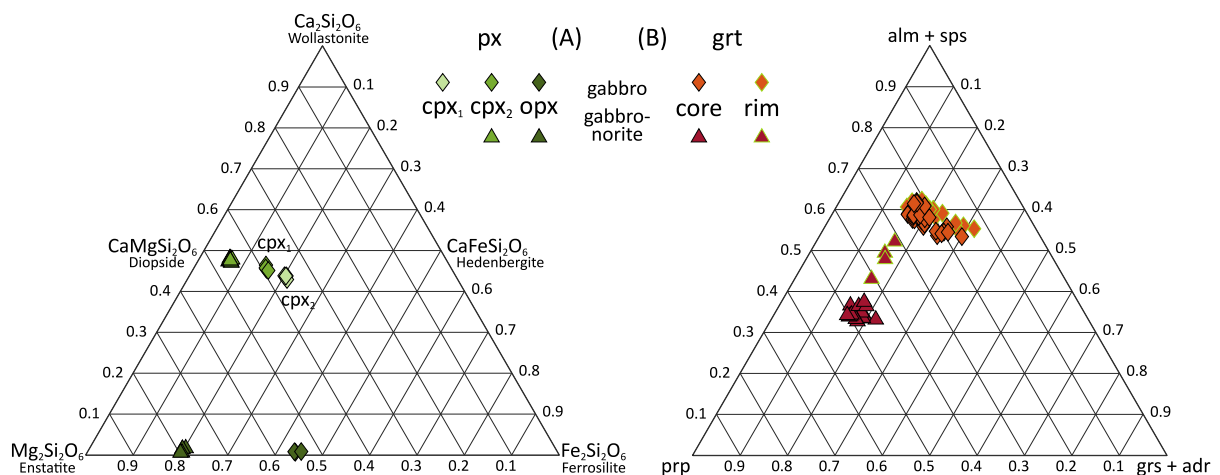


Figure 11: Ternary diagrams for (A) pyroxene and (B) garnet EMP measurements for both samples. Abbreviations: alm = almandine, sps = spessartine, prp = pyrope, grs = grossular, adr = andradite.

Pyroxenite

Aligning with field observations, the pyroxenite is slightly coarser grained than the dolerite, though the maximum grain size is still only around 10 mm. A compilation equivalent to the one for the dolerite (Fig. 2) is displayed in Figure 12, data analogous to Table 2 are listed in Table 5.

Amphibole forms the matrix in which pyroxenes, garnet, plagioclase, and occasional biotite are present. Notably, opaque phases are almost completely absent from the assemblage. All samples contain at least 30 vol% amphibole, but there is an increase towards the fracture to 46 vol% when averaging the first thin section (HU21), and 55 vol% maximum in the averaged modal abundances (Fig. 12C). The surrounding assemblage has less clinopyroxene (reduced from 10 to 5 vol%), slightly less orthopyroxene (from 38 to 28 vol%) and less plagioclase (from 13 to 7 vol%). Distance covered by a potential reaction related to the fracture is less obvious than in the dolerite, but the H₂O-curve (Fig. 12C, D) reaches a relatively constant level between 7 – 9 cm from the fracture, giving some indication how deep reactive fluid flow was able to penetrate the rock.

The main element bulk chemistry determined by SEM is marked by higher SiO₂ (55 wt%) and MgO (17 wt%) compared to the dolerite (50 wt% SiO₂, 5 wt% MgO), and lower Al₂O₃, FeO and Na₂O (Fig. 12D, Tab. 5). K₂O and TiO₂ are only measured in tiny amounts (< 0.3 wt%), as no high-Ti phase is present and biotite is sparse. There is stronger local fluctuation in main element concentration, related to heterogeneity in mineral abundances (e.g., higher Al and Ca where more plagioclase is present), but overall, the trend of water increase and slight decrease in Na₂O is present in this rock as well (Fig. 12D).

Table 5: Overview of mineral abundances, densities, and bulk compositions for the five thin sections made from the pyroxenite. Densities in g/cm³ at 720°C and 0.6 GPa. HU21 is closest to the fracture, HU25 furthest away. *Density calculated from EMP data and assumed constant over sample. Other values are calculated from averages of SEM data for each thin section.

	HU21		HU22		HU23		HU24		HU25	
	$\rho_{P,T}$	vol%								
qtz	2.57	5.31	2.57	4.76	2.57	3.95	2.57	4.24	2.57	4.32
plg	2.66	6.61	2.65	8.98	2.66	14.32	2.66	13.46	2.66	13.17
grt*	3.87	3.97	3.75	3.43	3.75	4.72	3.75	4.71	3.75	1.42
cpx*	3.26	4.97	3.26	6.45	3.26	10.35	3.26	11.64	3.26	10.15
opx*	3.32	28.13	3.33	36.52	3.32	32.88	3.32	34.42	3.32	38.26
amp*	3.04	49.10	3.04	38.38	3.04	33.39	3.04	31.03	3.04	31.90
bt	2.84	1.91	2.84	1.48	2.84	0.38	2.83	0.50	2.84	0.76
ρ_{tot}	3.11		3.12		3.11		3.12		3.11	
Bulk composition (wt%)										
SiO₂	55.89		55.88		55.65		55.77		56.13	
TiO₂	0.08		0.10		0.03		0.05		0.05	
Al₂O₃	9.35		8.88		10.08		9.69		8.80	
FeO^{tot}	8.74		9.15		8.48		8.64		8.91	
MgO	16.59		17.34		16.18		16.42		17.10	
CaO	7.70		7.11		8.06		8.00		7.53	
Na₂O	0.34		0.50		0.70		0.65		0.65	
K₂O	0.22		0.18		0.08		0.09		0.11	
H₂O^{calc}	1.09		0.87		0.73		0.69		0.73	

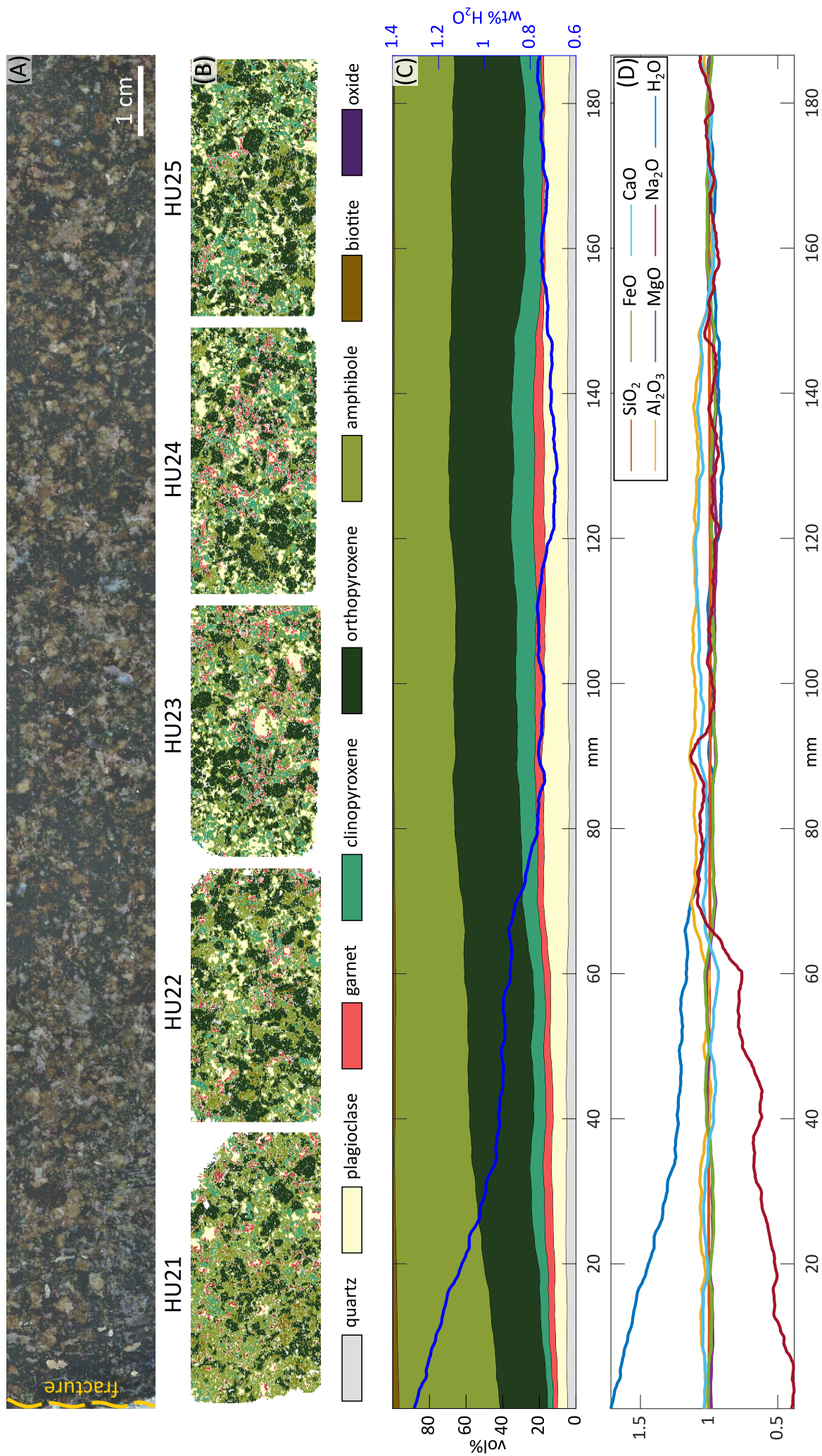


Figure 12: Overview of measurement results for the pyroxenite cross-section. Fracture observed in the field on the left. (A) Polished hand sample. (B) Phase maps of five thin sections cut from the sample, phase names indicated in legend below. (C) 1D average modal mineral abundance over the five thin sections, with calculated water content in the rock. (D) Relative concentration of main components over the five sections, normalized to average HU25 bulk composition.

Orthopyroxene

Orthopyroxene is the second major constituent of the rock after amphibole at 28 vol% at the fracture and up to 38 vol% in the less affected rock. It is present in relatively large, euhedral to subhedral crystals (Fig. 13A). The grain size decreases towards the fracture, indicating partial replacement by amphibole. The composition of about 79% enstatite and 20% ferrosilite (Tab. 4, Fig. 11A), with a minor Ca component reflects the much higher Mg/Fe ratio in this rock compared to the dolerite.

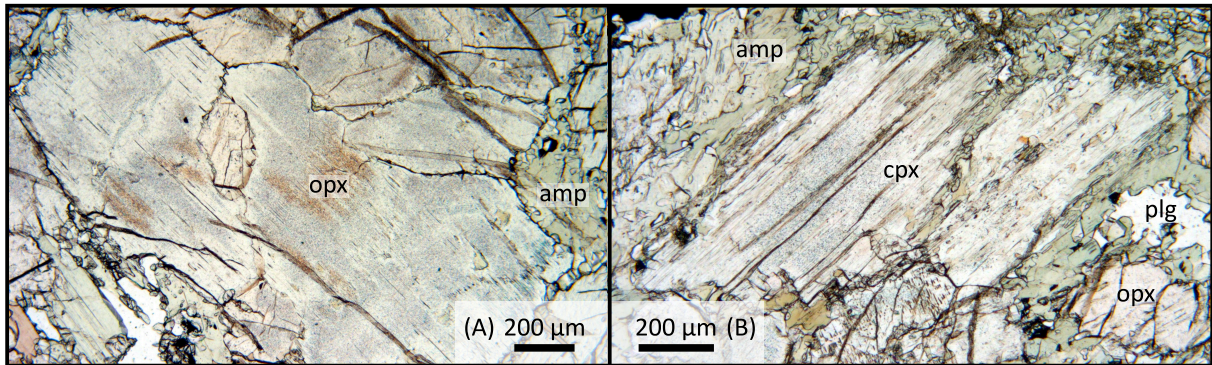


Figure 13: Polarized light images of (A) orthopyroxene and (B) clinopyroxene, both in thin section HU23, mostly unaffected by the investigated amphibolitization.

Clinopyroxene

Clinopyroxene is much less abundant than orthopyroxene (5 vol% at the fracture, 10 vol% further away), and there is only one generation of it in the pyroxenite. It is readily replaced by amphibole, commonly with some symplectitic quartz within the amphibole that forms, but this occurs less than in the pyroxenes from the dolerite dike. Clinopyroxene appears colorless in thin section (Fig. 13B), its composition is homogeneous at almost pure diopside (Tab. 4, Fig. 11A).

Amphibole

Amphibole is abundant throughout the cross-section, always forming at least a third of the rock volume and up to 55 vol% at the fracture. It appears anhedral as a matrix between the other phases (Fig. 14A) or in replacement coronas mostly around cpx (Fig. 14B), indicating its secondary nature. In the first thin section by distance to the fracture (HU21), a further increase in amphibole up to about 55 vol% is observed.

The amphibole present throughout the sample classifies as magnesiohornblende, with considerable compositional range, most pronounced in SiO_2 , Al_2O_3 , MgO and FeO contents (Fig. 7, Tab. 3). Where orthopyroxene is partially replaced by amphibole close to the fracture, Al content decreases and tremolite forms locally (Fig. 7, 15). At the edge of the first thin section, so as close as possible to the fracture within the samples, some hornblende grains contain the Ca-free amphibole cummingtonite, in small areas or along cracks within the grain. This is best visible in the BSE image, but also shows up as a very faint decrease in the intensity of green in thin section, visible with high contrast (Fig. 14 C, D). Splitting by Fe and Al content, this trend can be seen on the edge of thin section HU21 (Fig. 15).

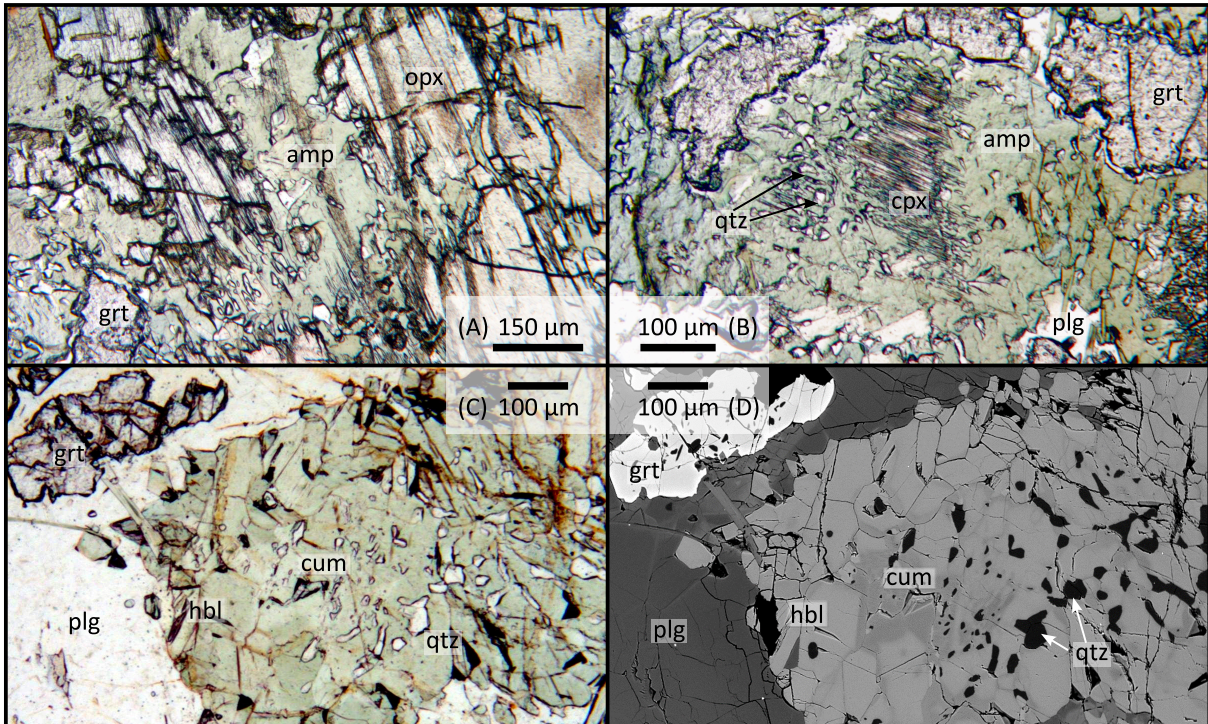


Figure 14: Polarized light images of (A) decomposing orthopyroxene in amphibole and (B) amphibole replacing clinopyroxene, with symplectitic quartz inclusions and a remnant clinopyroxene core. (C) Occurrence of cummingtonite, slightly paler than magnesianhornblende, very close to the fracture (< 5 mm). (D) BSE image of the same grain as in Fig. 14C, showing contrast between the two amphibole compositions. All on thin section HU21.

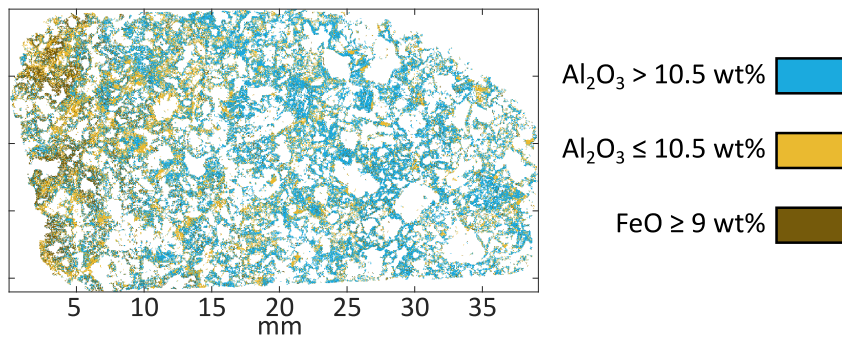


Figure 15: Distribution of amphibole compositions on thin section HU21, closest sample to the fracture on the left. A slight increase in low Al amphibole (trending towards tremolite) and high Fe, low Ca amphibole (towards cummingtonite) is visible on the first few mm of the thin section.

Plagioclase

Plagioclase in the pyroxenite does not show an increase in Ca close to the fracture like in the dolerite. It appears mostly anhedral and as relatively small grains (~1-2 mm, Fig. 16A). Locally, larger grains (~5 mm) are present (Fig. 16B). Plagioclase abundance fluctuates between 5 and 15 vol%, related to the layering of the pyroxenite body. In some areas, quartz also occurs together with garnet and feldspar (Fig. 16B), which is otherwise present in symplectitic intergrowth with amphibole around replaced clinopyroxene.

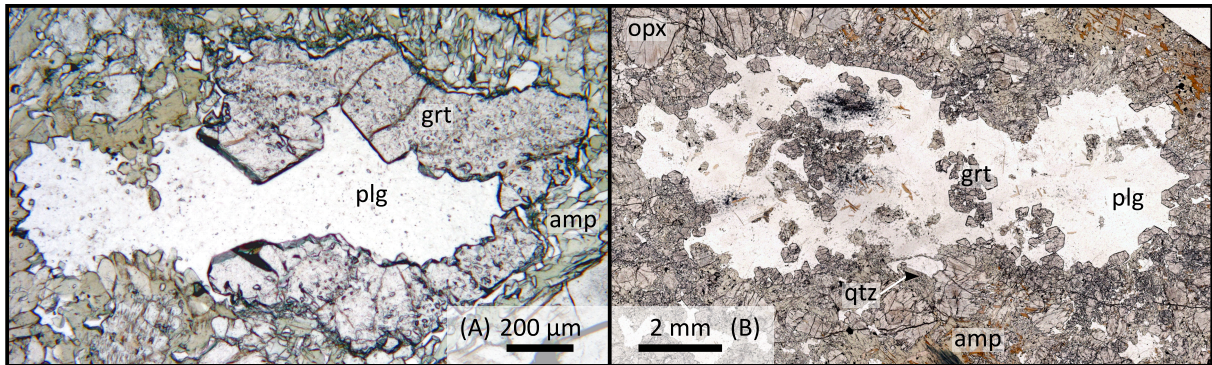


Figure 16: Polarized light images of plagioclase and garnet in the pyroxenite. (A) Small grain in thin section HU23, half surrounded by garnet. (B) Large grain in thin section HU27, with small (<1 mm) garnet grains adjacent to large parts of the grain and some garnet within it. Also, a ca. 1mm grain of quartz is present next to the plagioclase.

Garnet

Garnet appears throughout the samples and almost exclusively together with plagioclase and often surrounding it (Fig. 16), recording previous metamorphic reactions on the boundary of plagioclase with amphibole or pyroxene. Like plagioclase, garnet abundance fluctuates over the sample, from 1 up to 5 vol% (Fig. 12B, C, Tab. 5). This fluctuation appears to be unrelated to the fracture and reaction zone. However, garnet also shows Mn-rich rims close to the fracture, like in the dolerite dike. Here, the previous pyrope rich garnet is transformed to almandine-rich with a much bigger spessartine component (Tab. 4, Fig. 11B), marked by a drop in Mg and simultaneous increase in Mn and Fe on the EMP map (Fig. 17). Overall, the garnet in this lithology is pyrope rich and almandine poor compared to the dolerite, again indicating the difference in Fe/Mg ratio in the bulk composition (Fig. 11B).

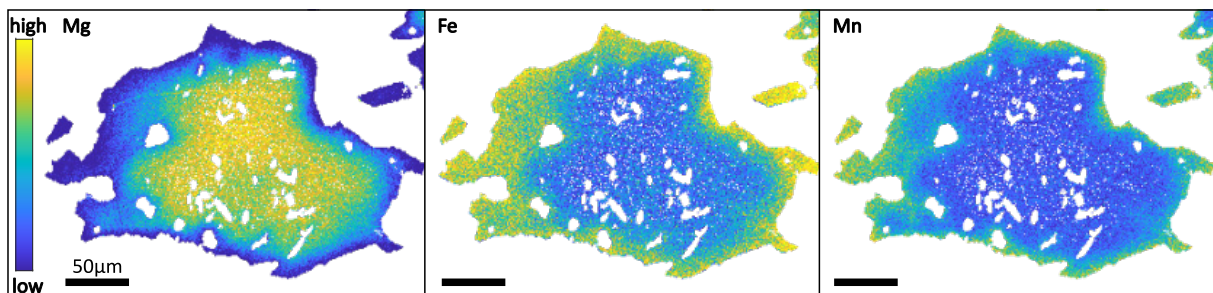


Figure 17: Zonation in garnet close to the fracture in the pyroxenite. Mg decreasing, Fe and Mn increasing from core to rim. Thin section HU21.

Modeling Results

Constraining Pressure and Temperature

To enable numerical modeling of the amphibolitization of the two described lithologies, the physical conditions during the process need to be determined, to be combined with chemical composition and employed in the system of equations (eq. XIII, XIV) described above. This is achieved by matching the measured mineral paragenesis of the forming rock to phase equilibria calculated with Thermolab. For the thermodynamic calculation of P/T phase diagrams, the bulk composition of the thin section closest to the fracture of the two samples (HU01, HU21) was used (Tab. 2, 4). This composition was determined by averaging the data generated by the SEM for the whole thin section.

Electron microprobe analyses yield different results for mineral chemistry, most notably lower SiO₂ concentrations in amphibole due to small scale intergrowth with quartz, unresolvable in the SEM setup. But the occurrence of mixed analysis has no impact on the accuracy of the determined bulk composition of any given 40x40 μm pixel on the maps. Uncertainties on individual points may be greater in the SEM measurements, but there are orders of magnitude more points available from this dataset compared to the EMP, meaning these measurements have no thin-section-scale sampling bias, as EMP data inherently would. Additionally, there is a huge compositional range in the amphiboles (Fig. 6, 7, Tab. 3), which makes it hard to determine an average composition from just point measurements. As mentioned before, MnO was omitted from the calculation because it does not appear in the solution model of any phase actually present in the rock.

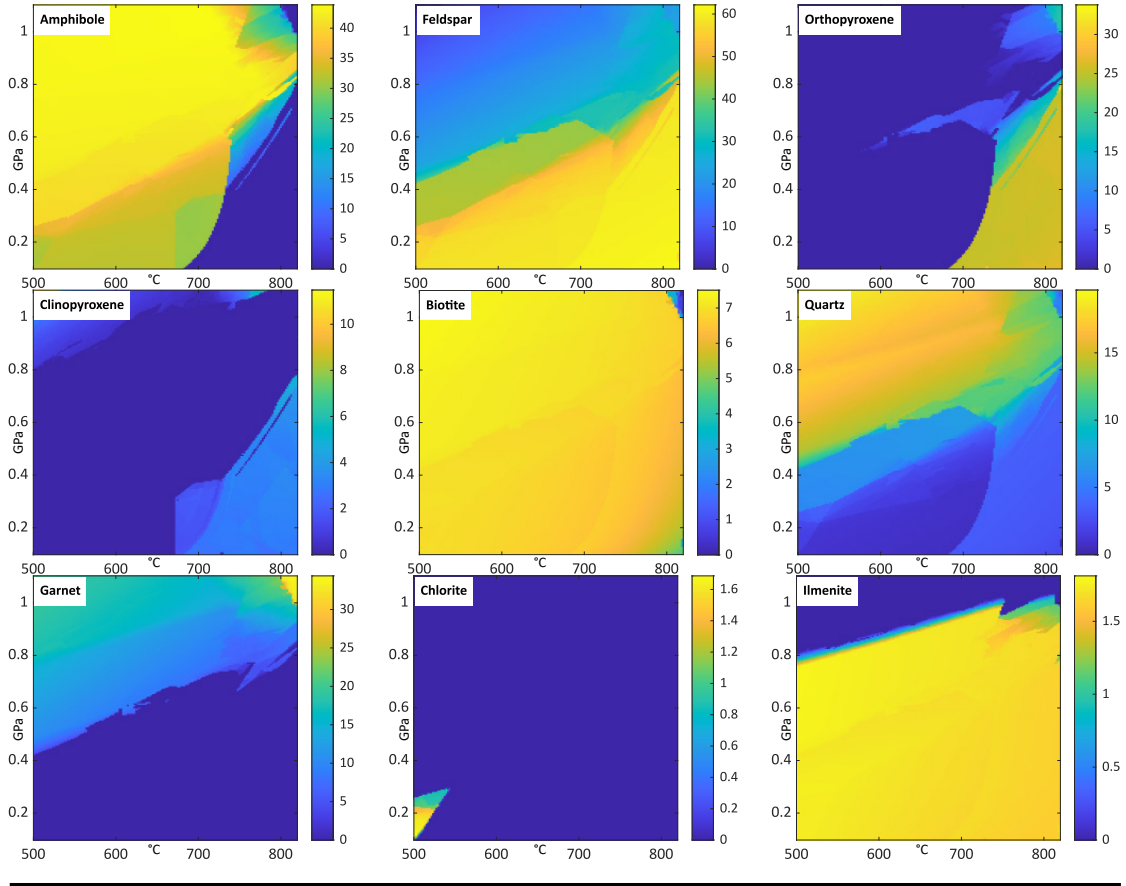
Both compositions were entered into Thermolab with and without excess H₂O and abundances of relevant phases attained by Gibbs energy minimization are presented in Figures 18 and 19. The stability of garnet with sufficient pressure and pyroxenes with sufficient temperature in the dolerite, the latter coinciding with amphibole breakdown at lower pressures, supply initial constraints on the conditions during amphibolitization (Fig. 18). A further upper limit is imposed by the high abundance of quartz in the high P, low T regime of the investigated P/T-range. These observations are combined in Figure 20A, with maxima of ca. 0.6 GPa and ca. 730°C.

The same calculation for the pyroxenite (Fig. 19) shows that, with excess fluid available for reaction, chlorite and talc would be stable up to 600 – 730°C, depending on pressure. As neither are observed anywhere in the rock, conditions must be outside of their stability fields. Combining with the much too high abundance of feldspar in lower pressures and absence thereof at higher pressures, a field of possible conditions can be drawn (Fig. 20B).

The overlap of the two fields indicates where both assemblages that are presumed to have formed in the same event would be stable in principle, thus providing a window of possible PT-conditions: 0.4 – 0.6 GPa and 650 – 730°C. Plagioclase abundance in the pyroxenite is closest to measurement where it is lowest in this window, which is at both higher T and P. Thus, the best estimate for amphibolite formation in these rocks is around 720°C and 0.6 GPa, which will be used in the reactive transport model.

Including excess fluid in the pyroxenite composition leads to an increase in amphibole abundance, exceeding 80 vol% in some areas and around 70 vol% in the best fit area, while orthopyroxene is only stable in this field without excess fluid (Fig. 19). This issue would not be present at higher temperatures, where there is an overlap of stability of amphibole and orthopyroxene, but either garnet or orthopyroxene would be stable in the dolerite under these conditions (Fig. 18), opposing observation. This indicates that the measured sample of pyroxenite never reached water saturation.

Calculated modal abundances for dolerite bulk composition (HU01)



With fluid in excess

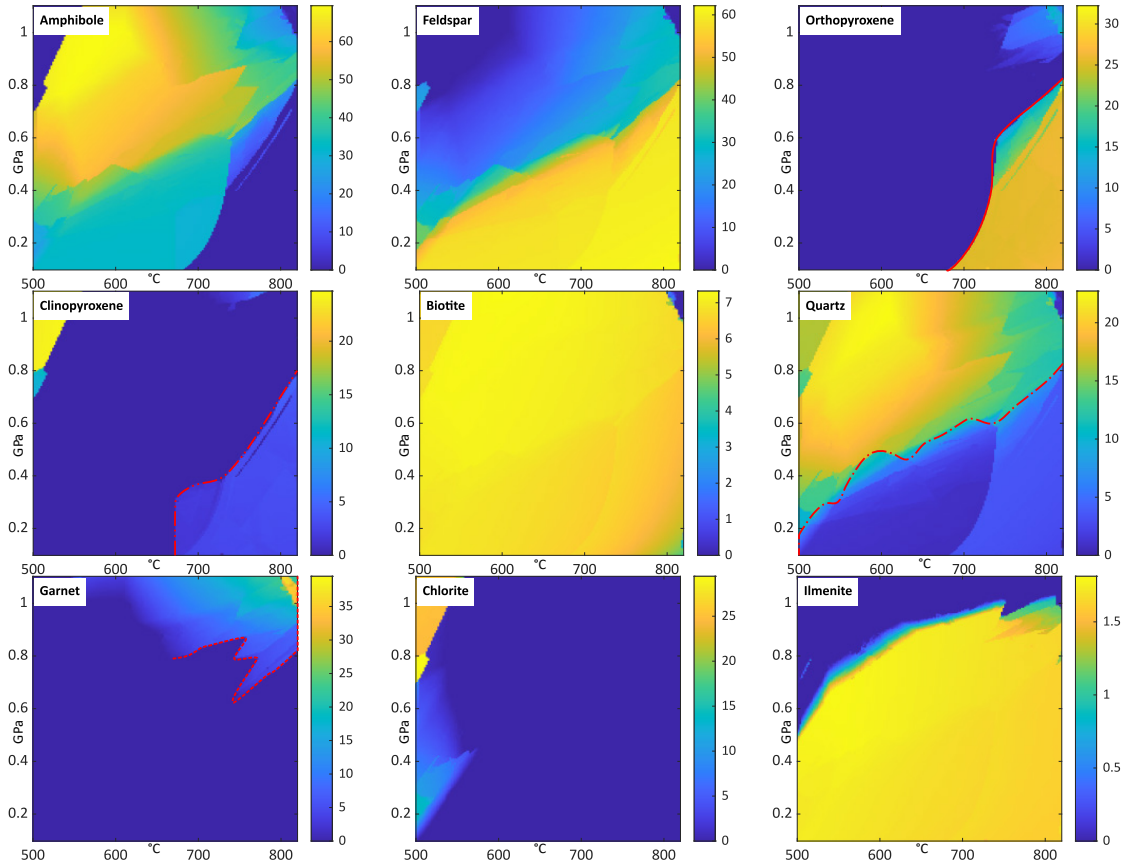
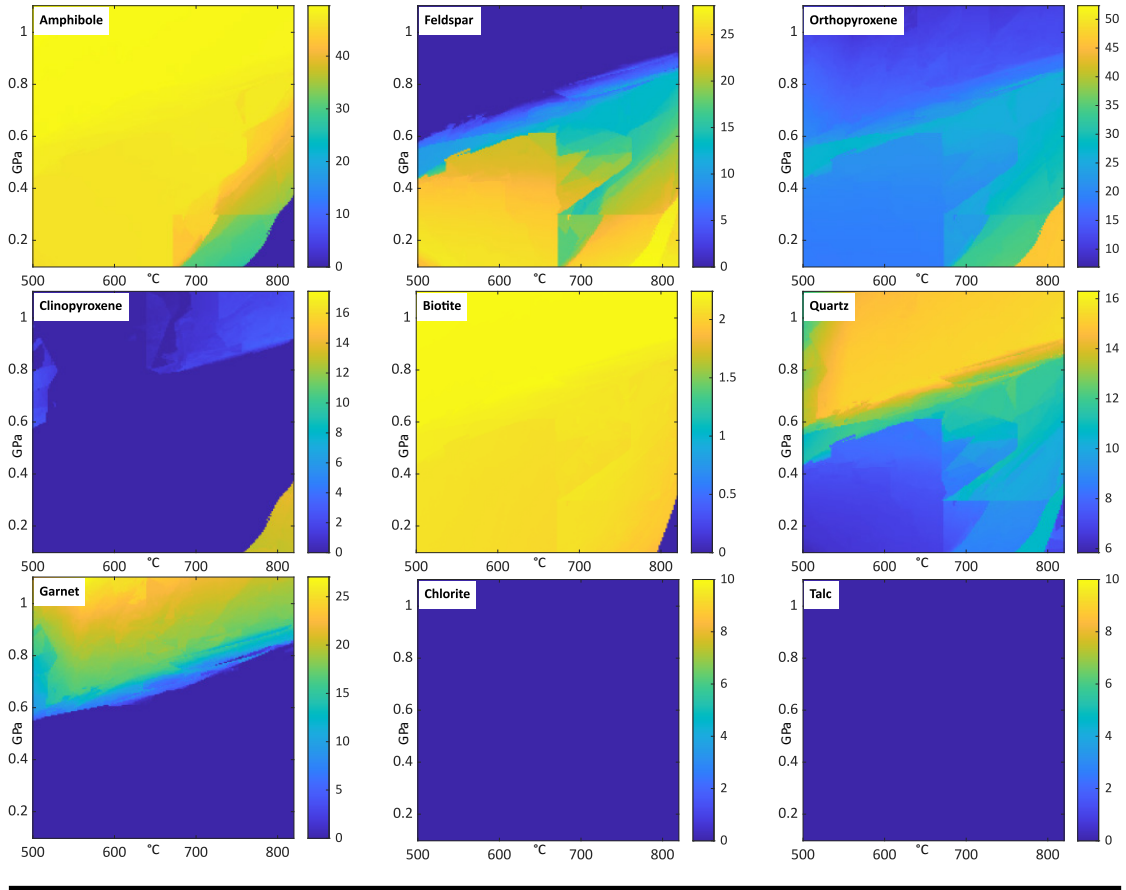


Figure 18: Phase abundance (vol%) diagrams for the dolerite, without (top) and with (bottom) excess H₂O, for relevant phases. Color bars indicate volume percent range of each phase. Lines drawn are used to construct P/T window in Figure 20.

Calculated modal abundances for pyroxenite bulk composition (HU21)



With fluid in excess

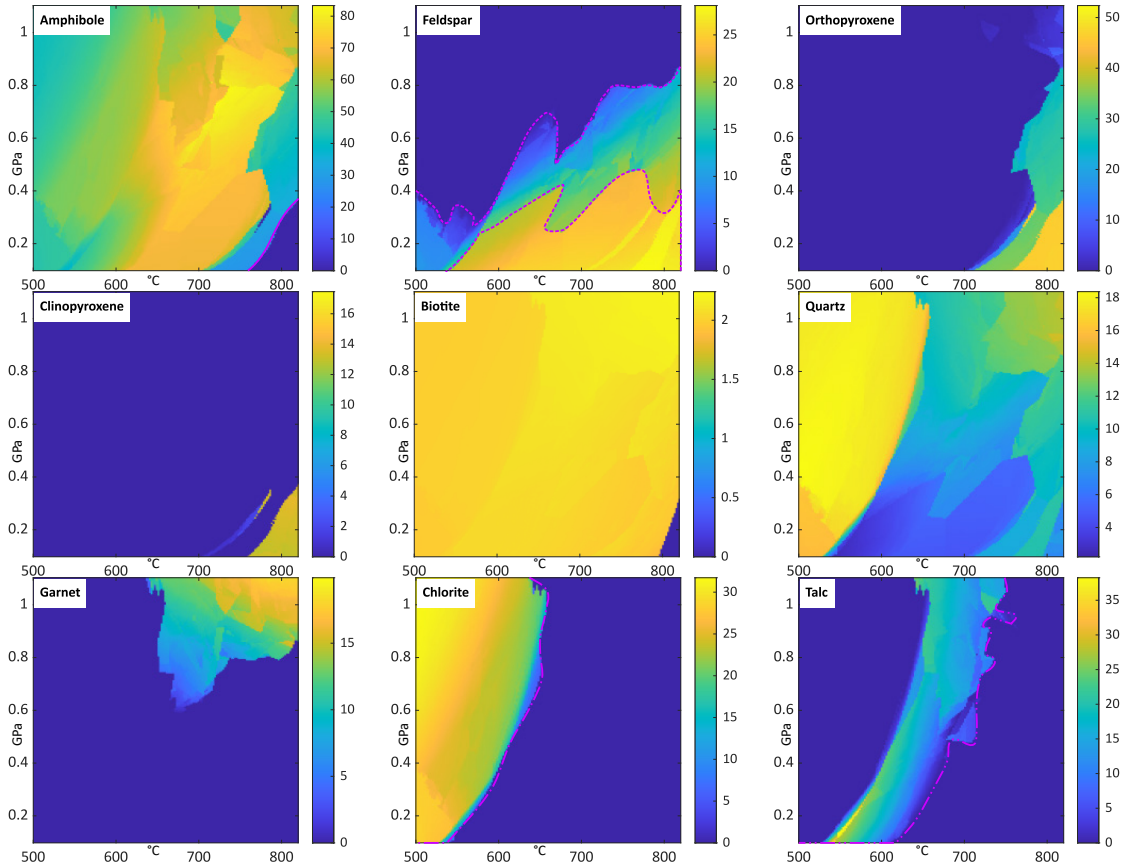


Figure 19: Phase abundance (vol%) diagrams for the pyroxenite, without (top) and with (bottom) excess H₂O, for relevant phases. Color bars indicate volume percent range of each phase. Lines drawn are used to construct P/T window in Figure 20.

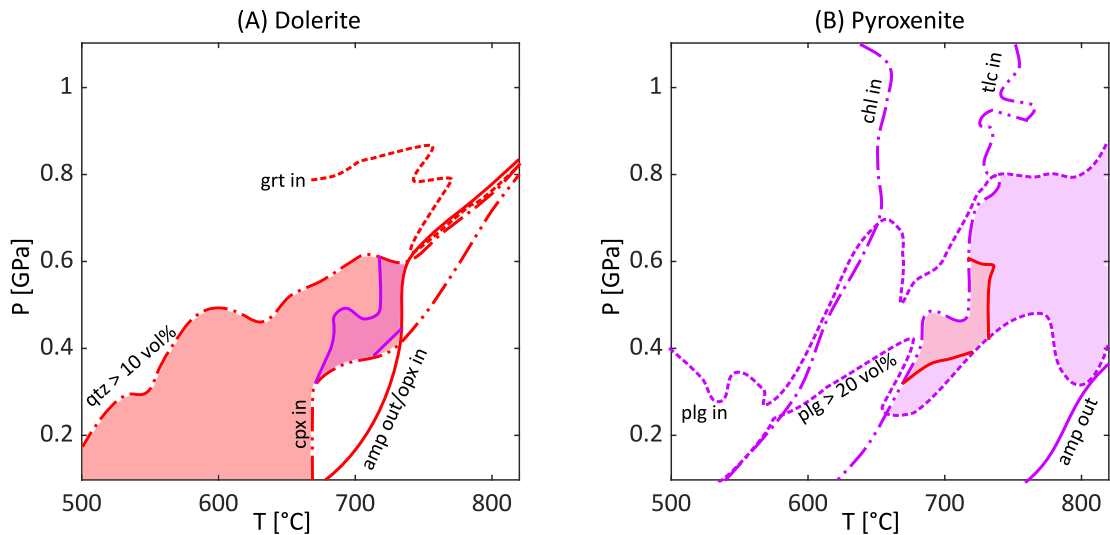


Figure 20: Combined constraints on P/T-conditions for amphibolitization of (A) dolerite and (B) pyroxenite, resulting from phase diagrams (Figs. 18, 19). Window of overlap indicated on both plots.

Reactive Fluid Flow Models

Stable mineral assemblages calculated with Thermolab from measured bulk compositions of either rock type with fluid in excess are displayed in Figure 21, at constant temperature (720°C) and over a range of pressure around 0.6 GPa, to best reproduce the measured mineral paragenesis of the real rocks (Fig. 18 – 20). The range indicated on the figure represents the minimum and maximum values of fluid pressure used in the reactive transport model (0.58 – 0.6 GPa). For both bulk compositions, calculated solid density and amphibole abundance increase with higher pressure, indicating a positive Clapeyron slope for the hydration reaction under these conditions (Malvoisin et al. 2015), with amphibole abundance serving as a proxy for bulk rock water content. Both gradients are steeper in the dolerite.

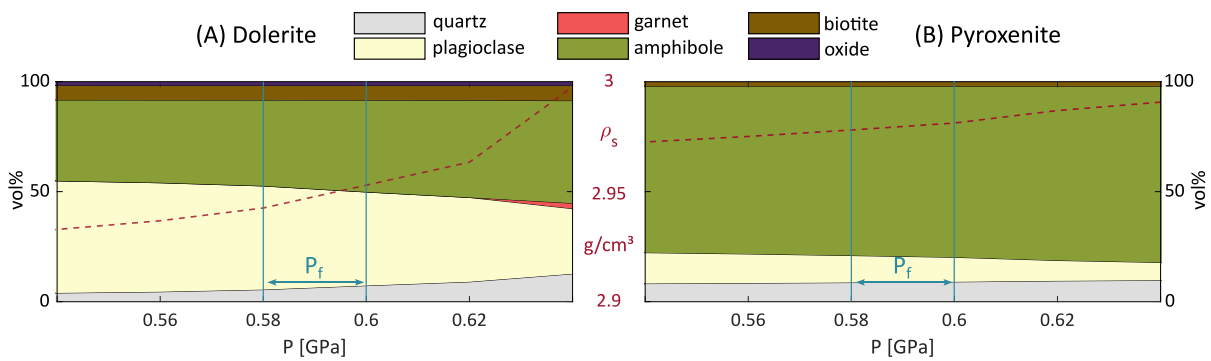


Figure 21: Calculated (Thermolab) mineral modal abundances at constant temperature (720°C) over variable pressure for bulk compositions with fluid in excess of (A) dolerite (HU01) and (B) pyroxenite (HU21). Calculated solid density indicated by red dashed lines, fluid pressure range applied in the reactive transport model marked by blue lines.

Diagrams showing the evolution of fluid pressure, porosity, and mineral abundances in the model for both rocks are presented in Figure 22. Fluid flow occurs following the pressure gradient (eq. VII, XIII).

Analogous to the real samples, the initial assemblages are replaced, increasing the amphibole and water content in the rocks, accompanied by formation of some quartz (Fig. 22C). Garnet and pyroxene disappear in both lithologies, consistent with observed mineralogy of the dolerite (Fig. 2). With complete fluid saturation, pyroxenes are calculated to be unstable in the pyroxenite under the

determined conditions (Fig. 20). Thus, the stable assemblage calculated for the evolution of the reactive fluid flow model does not contain these minerals.

In the way the model is set up, the change in mineralogy is instantaneous, because the reaction is assumed to fully occur as soon as fluid is in contact with the rock. This results in a very sharp front in mineral paragenesis, while fluid pressure and porosity evolve along a more diffusive path.

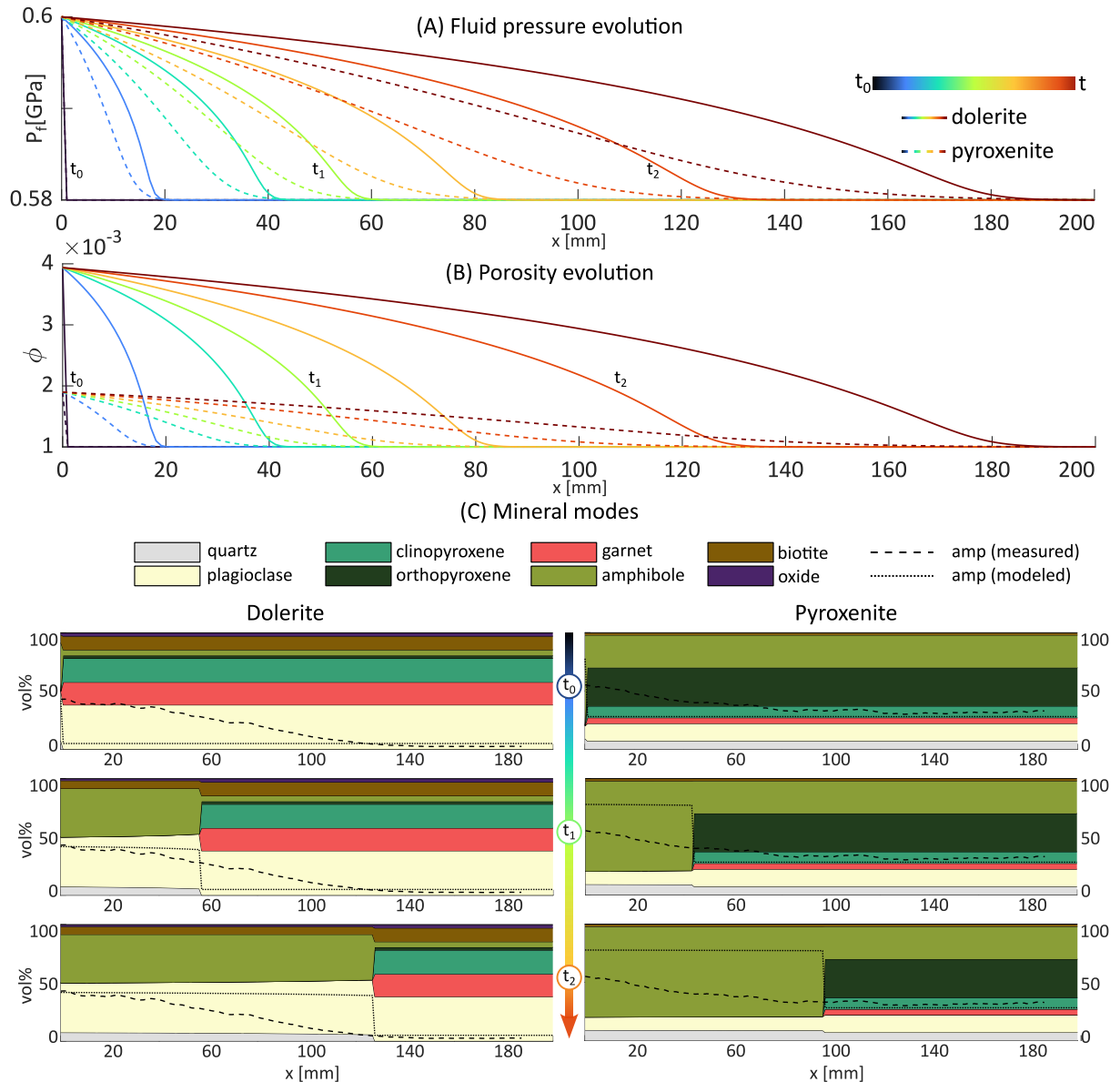


Figure 22: Results of the 1D-reactive fluid flow model. (A) Evolution of fluid pressure P_f over the duration of the model, initial conditions and six snapshots at increasing timesteps. (B) Evolution of porosity at the same timesteps. (C) Mineral modal abundances at t_0 , t_1 and t_2 , as indicated in (A) and (B), including a comparison of measured and modeled amphibole abundance for both lithologies.

Discussion

The described samples provide a unique look into the onset of lower crustal hydration at depth. The difference in reactional progress in the two lithologies indicates differences in reaction front propagation velocity under exposure to the same fluid under the same physical conditions.

Reactive Fluid Flow Through a Solid Polygranular Medium

The presence of hydrous phases replacing the previous, in the case of the dolerite mostly dry assemblage, is unambiguous evidence of a fluid infiltration event. Evidence of two different mechanisms governing fluid flow through practically impermeable rock are preserved in the investigated samples:

The first are interface coupled dissolution-precipitation reactions, where minerals are dissolved only along a very narrow front and the new, stable assemblage reprecipitates continuously behind this front with nanoscale transient porosity as a means of fluid flow (e.g., Putnis and John 2010, Putnis and Austrheim 2010, Plümper et al. 2012, Ague and Axler 2016). On the other hand, fluid flow has been shown to occur along grain and phase boundaries in parallel to dissolution-precipitation on individual grains, allowing for faster front propagation (Jonas et al. 2014, Wirth et al. 2022). Grain boundary flow has also been shown to follow paths that result in the maximum gain in Gibbs free energy (Zertani et al. 2022). As a result, reaction fronts can move forward along grain boundaries before pervasive replacement of all grains is complete, and a transition zone of incomplete replacement appears.

This is exactly what is observed in the dolerite sample: Complete replacement of individual grains, marked by full, pseudomorphic amphibole growth after clinopyroxene does happen in the rock, but fluid continues flowing before the reaction is complete.

Amphibolitization Mechanisms in the Different Lithologies

Dolerite

Within the reaction halo in the dolerite dike, nearly the whole rock is progressively altered from the original paragenesis. Pyroxene and garnet are replaced with amphibole, feldspar composition changes completely and pervasively. All stages of this are observable in the samples. Texturally however, the original rock is well preserved, with no clear development of an orientation of minerals or deformation textures. Amphibole grows in the shape of the clinopyroxene it replaces, plagioclase recrystallizes as a fine-grained aggregate, but initial grain boundaries are still recognizable. The already fragmented cpx_2 is fully replaced by amphibole and an amphibole-quartz symplectite before replacement of the bigger cpx_1 grains is complete. Replacement of plagioclase occurs first in areas close to dissolving garnet and pyroxene but is observed everywhere in the samples closest to the fracture, indicating that initial flow occurs primarily along phase boundaries. A qualitative sketch of this process, showing three stages (protolith, incomplete and complete replacement) is shown in Figure 23.

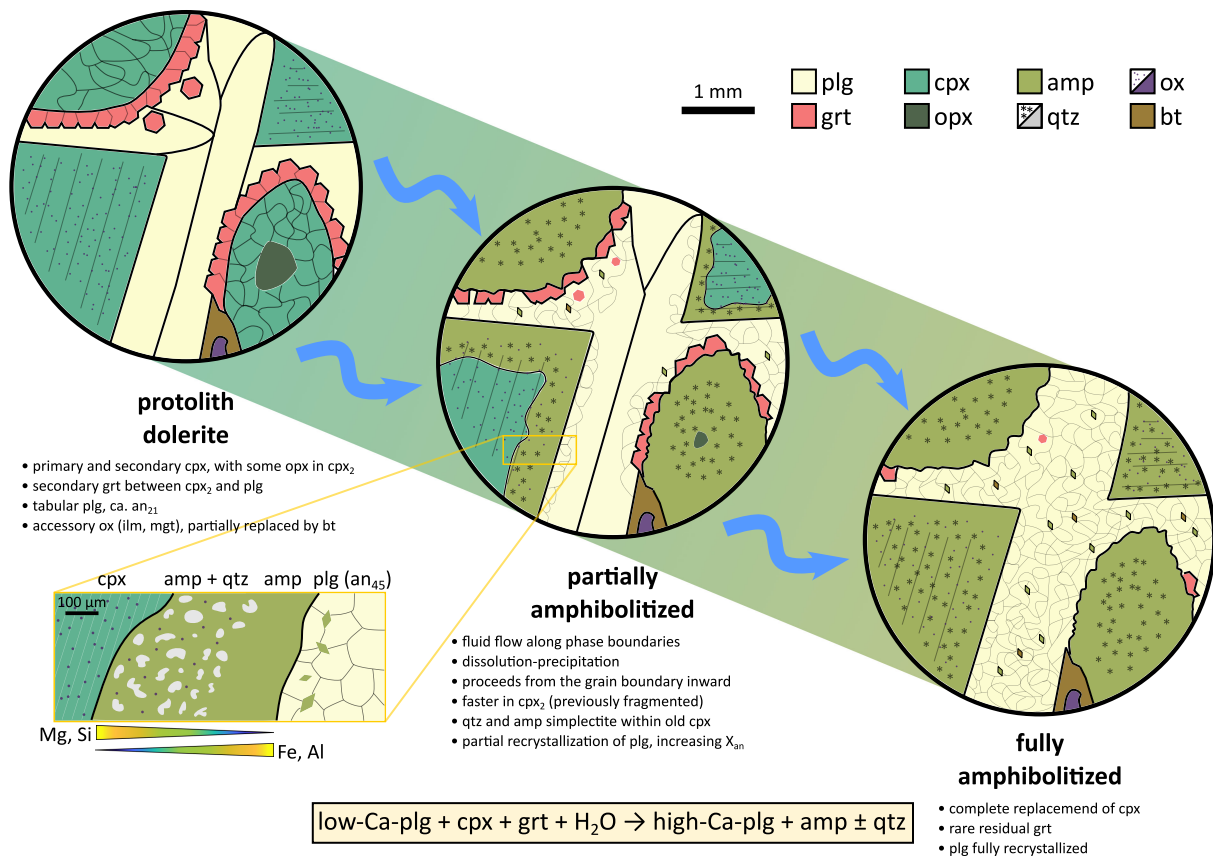


Figure 23: Sketched three-stage evolution of the dolerite during amphibolitization by reactive fluid flow along grain boundaries and dissolution-precipitation within grains, including detail sketch of partial amphibolitization of clinopyroxene with indicated chemical gradients in amphibole analogous to Figure 6.

While amphibole appears in pyroxene pseudomorphs, it is not simply formed by the addition of water. Mg and Fe are added from dissolving garnet and local excess Si precipitates as quartz. Ca, high in clinopyroxene but low in amphibole, is moved into the new plagioclase. In essence, all main phases within the dolerite react simultaneously to form the new assemblage, following the qualitative equation in Figure 23.

Amphibole composition shows a gradient from the grain boundary to the core (Figs. 4 – 7, Tab. 3), indicating that the elements provided by consumption of garnet are limited in their mobility into grains. The occurrence of quartz-amphibole symplectites in amphibole cores further documents limited fluid-mediated element transport. This creates an issue for the simplification to one spatial dimension for both analytical results (Fig. 2) and numerical modeling (Fig. 22), because local availability of elements and fluid pathways decide which amphibole forms and if dissolved SiO₂ is transported away or contained on site.

Density Evolution

According to the thermodynamic calculations using measured compositions, there is a decrease in bulk rock density from ca. 3.2 (dolerite) to ca. 3.0 g/cm³ (amphibolite) (Tab. 2). This is equivalent to a volume increase of ca. 7%, mainly due to the dissolution of high-density garnet. The forming amphibole has a lower density than the clinopyroxene, but this is counteracted by the density increase in plagioclase due to anorthite enrichment, which is the only relevant densification involved. As low-density water is incorporated into the rock, the total amount of expansion needed will be slightly lower than it seems when just comparing solid densities. Nevertheless, a volume increase is predicted for the combined

reaction, which should clog forming porosity if there is no deformation or change in total volume or mass. One of the most well-known metasomatic reactions, the formation of serpentine from olivine and water, results in volume increases of up to 30% (e.g., Bach and Früh-Green 2010), but massive peridotite bodies are still commonly pervasively serpentinized, often with pseudomorphs after olivine. So, pervasive hydration reactions with simultaneous solid expansion are far from unheard of.

The expansion could be accommodated by deformation, indicated by features such as cracks or shear zones, not observed in the sample. Experiments on plagioclase-pyroxene mixtures under similar conditions to those observed here indicate that most strain is accommodated by grain boundary sliding and dissolution-precipitation creep (Marti et al. 2018), though the samples in that study were subject to shear stress, while the samples investigated here only experienced pure tensile stress.

A change in solid mass to accommodate the higher specific volume would be an explanation by which this transformation took place, and there is a decrease in Na content measurable in the samples (Fig. 2D, Tab. 2), while other main elements stay roughly the same. However, the removal of small amounts of Na would not result in a mass-loss significant enough to accommodate a volume increase of 7% and no other significant component shows a relevant change.

A fluid filled or at the very least highly permeable fracture was present during the reaction and served as fluid source. In theory, the extension required for such a fracture could accommodate the generated volume. This may also be an explanation for the small scale of the reaction, stopping due to fluid pathways clogging up, and stopping earlier where the width of the fracture currently observed by pegmatite filling is small. E-W extension has been shown to be an important part of the Western Gneiss regions exhumation, and amphibolite facies metamorphism along this path is recorded throughout the region and the Scandinavian Caledonides (Hacker et al. 2010, Corfu et al. 2014), so solid expansion to accommodate the density decrease was certainly possible when the reaction happened.

Another key observation may be the complete reworking of plagioclase in the rock, as feldspar has been found to be a good medium for pervasive fluid flow (Plümper et al. 2017b), and in this case it is obvious that the number of grain boundaries within the mineral increases drastically (Fig. 8, 23), potentially further amplifying its ability to facilitate fluid flow. The small size of the forming plagioclase may also allow for an easier accommodation of volume increase, because grains can more easily move relative to each other along the fluid-lubricated grain boundaries.

Pyroxenite

In the pyroxenite, a question needs to be answered before discussing reactional mechanisms: Did the amphibolite facies event that transformed the dolerite affect the surrounding pyroxenite much stronger than the dolerite, or are there separate amphibole forming events recorded in the rock? While the change in paragenesis is quite easily visible in hand sample in the dolerite, it is less straightforward in the pyroxenite.

The entire sample contains at least 30 vol% amphibole, which only appears as a matrix between partially dissolved pyroxene grains, with slightly stronger replacement of clino- compared to orthopyroxene, clearly pointing to a secondary origin. However, there is an increase in abundance towards the fracture up to 55 vol% (Fig. 12C). As this is the only clear change in amphibole content over the sample, heterogeneity in mineral distribution as with plagioclase or garnet is ruled out as the cause of the gradient. There is a similar gradient in measured Na₂O and calculated H₂O concentration in the sample (Fig. 12D), indicating fluid penetration of 60 – 80 mm.

Very close to the fracture ($x < 2$ cm), there is also a partial change in amphibole composition towards more Fe/Mg-rich endmembers (Figs. 7, 14, 15, Tab. 3), possibly indicating replacement of orthopyroxene. Similarly, garnet only has Mn-rich rims close to the fracture (Figs. 11, 17, Tab. 4), matching with the dolerite (Fig. 10). All of these indicate that the event that transformed the dolerite is also observed in the pyroxenite with a slightly smaller halo, and some amphibole was formed in previous, pervasive metamorphism.

The intrusion of the dike has been dated (1.25 Ga, Austrheim et al. 2003), so has the formation of the spatially related granitic body (1.65 Ga), already leaving a minimum of 400 million years between formation of pyroxenite and dike. The relationship between pyroxenite and granite is not certain, and while it could be a cumulate from the same melt, it may also be part of a much older body, which would open a window of potentially billions of years for metamorphism predating the rest of the HIC and most importantly, the dolerite dike.

P/T-conditions determined for the observed reaction in the dolerite do not allow coexistence of amphibole and pyroxene in the pyroxenite (Fig. 20) when fluid is available in excess, but even at the fracture itself, orthopyroxene is still abundant and there are quite a few clinopyroxene cores left that have not been fully replaced (Fig. 12B, C). This is due to a stronger difference in fluid propagation speed between grain boundary flow and dissolution-precipitation compared to the dolerite, and the amount of pyroxene left in the affected rock is a function of this difference. Orthopyroxene also seems to be more resistant to replacement, slowing down full rock transformation.

In conclusion, previous metamorphism is favored as an explanation for most amphibole, but about 6 – 8 cm of the sample are interpreted to be affected by the event that is in the center of this study. The main control on front propagation is grain boundary assisted fluid flow, and replacement by dissolution-precipitation of single grains plays a minor role, less than in the dolerite.

The clear decrease in density observed over the dolerite sample is not present in the pyroxenite (Tab. 4) because there is only minor change in mineral paragenesis throughout the sample, and no relevant compositional gradient in the minerals to result in a gradient in density. Constant density should theoretically make porous flow easier and thus faster, as existing porosity would not be filled by expanding rock volume. Exactly the opposite is observed, the reaction proceeded further in the dolerite.

Differences Between the Two Transformations

In the field, reaction halos around the pegmatite filled fractures show variable thicknesses, roughly proportional to thickness of the pegmatites themselves. Both samples were taken at about equally thick pegmatite filled fractures and close to each other, but not on the exact same fracture. Sampling bias can thus not be excluded as an explanation for the thinner halo in the pyroxenite.

Despite that, arguments can be made to explain the observed difference: Plagioclase plays a significant role in the transformation of the dolerite and as a fluid transport medium and is scarce and barely taking part in reaction in the pyroxenite. Amphibole is already abundant in the pyroxenite before fluid infiltration at the fracture, and likely not too far from stable composition. This amphibole forms a matrix around metastable pyroxenes, garnets, and plagioclases, shielding them from the reactive fluid and inhibiting progress. Additionally, orthopyroxene seems to be much more resilient against the replacement compared to clinopyroxene in the pyroxenite. As orthopyroxene is almost absent from the dolerite, this is another issue that is only present in the rock with less reactional progress.

Combining these observations, reactions in the pyroxenite would likely result in a much lower energy gain compared the dolerite to amphibolite transformation. Reactions in the dolerite are thus favored at the outcrop scale, analogous to findings of Zertani et al. (2022) at the grain scale. With its slightly larger grain size, the pyroxenite also has fewer grain boundaries that serve as fluid channels.

Interpreting the Model Results

Influence of Bulk Rock Properties

The numerical model of porous flow shows that a reactive fluid in local equilibrium with the surrounding rock can propagate an amphibolitization reaction through both investigated lithologies. A fluid pressure gradient can drive the reaction forward through porous flow, and continuous fluid supply to the front is ensured by increased porosity under higher fluid pressure.

Bulk rock properties influence the velocity of front propagation. Reactive fluid flow occurs faster (i.e., over fewer numerical timesteps) with dolerite bulk composition, because the porosity increases to a maximum of ca. $3.9 \cdot 10^{-3}$, and only to ca. $1.9 \cdot 10^{-3}$ when modeling with the pyroxenite composition (Fig. 22A, B). This reduces Darcy flux (eq. VII), slowing down fluid flow. Initial porosity was the same in both models at 10^{-3} , and so were all other parameters aside from the bulk rock composition.

This difference in porosity is dictated by thermodynamics: Under constant temperature and exposed to the same pressure gradient, the gradient in density of the forming rock is steeper in the dolerite and more water is incorporated into the solid (Fig. 21), allowing for a greater volume decrease and formation of more porosity.

Shape of the Reaction Front

The modeled reaction front is extremely sharp, occurring between only two numerical grid points, where one contains the old, “metastable” assemblage and the next has the assemblage calculated by equilibrium thermodynamics, as the reaction is assumed to occur instantaneously once the fluid is in contact with the rock. This would occur independent of point spacing or scale of the model, and can be interpreted in multiple ways:

1. Kinetic factors are not considered, while the observed samples clearly show a gradual transition between unstable and stable assemblage. To fix this, the model could include a reaction rate for interpolating mineral modal abundances (e.g., Malvoisin et al. 2021) and the assumption of instantaneous transformation is wrong.
2. The model has a scale limitation, below which the applied system of equations cannot sufficiently explain how things evolve. Judging from a few meters distance, the observed front in the real rocks also looks quite sharp. Only when looking more closely and after post-processing measurements, the diffusive nature of the front is revealed to the observer.
3. There is a dimensional problem: The examined hydration reactions occurred in three-dimensional space, simplified to 2D by the sampling method and measurement and further simplified to 1D by averaging. The model on the other hand only describes evolution in one-dimensional space. In the real samples, grain boundary flow occurs faster than replacement of individual grains by dissolution-precipitation. This approximately bimodal speed of reactive fluid flow cannot be captured in the 1D-model and allows the front, defined by the furthest point from the fracture where metasomatism has occurred, to progress before complete equilibration. It also implies that more fluid is available at the grain boundaries than can be consumed to form hydrous phases, enabling flow in parallel to reaction and supporting the assumption of excess fluid in local equilibrium.

In the end, it may be a combination of these three that cause the discrepancy between model and observation. However, explanation three is easiest to fix without further assumptions:

This can be demonstrated by applying the same equations (eq. XIII, XIV) to a simple 2D-model, replacing the x-derivatives with gradients (Beinlich et al. 2020, Huber et al. 2022) and applying it to a highly simplified domain with rhomboid, equally sized grains and connected boundaries, defined by differences in initial porosity φ_0 (10^{-4} in grains, 10^{-2} on boundaries). This way, higher permeability along grain boundaries as observed in the samples is translated into the model (Fig. 24). After re-averaging to 1D and smoothing the result just like the real data, a gradient in the abundance of the new assemblage is observed, while each individual point in the grid is still in a binary (reacted/not reacted) state. This also demonstrates that the previous 1D model applies well to any individual hydrating pyroxene grain, where the transition from pyroxene to amphibole itself is just as sharp as in the model, and gradual transition only occurs behind this front (Fig. 6).

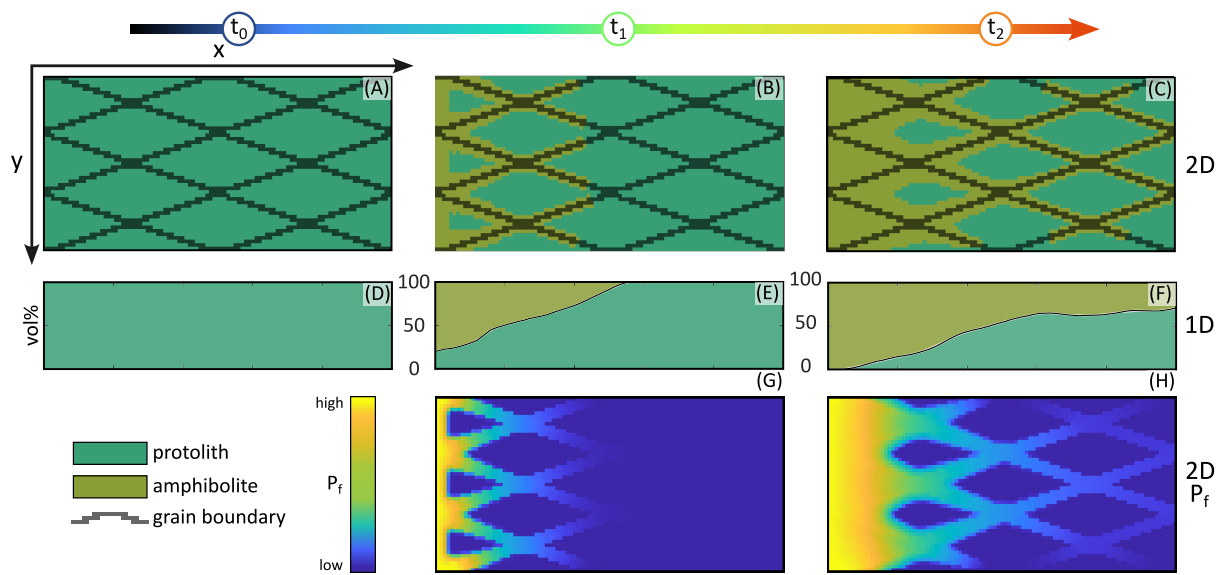


Figure 24: Results of 2D reactive transport modeling in a simplified domain with rhomboid grains ($\varphi_0 = 10^{-4}$) and more permeable grain boundaries ($\varphi_0 = 10^{-2}$). (A) Initial state of protolith with marked boundaries. (B, C) State of reactional progress at two later timesteps. (D-F) 1D-average of reactional progress between protolith and amphibolite in volume percent at the same timesteps as A-C. (G, H) 2D-images of fluid pressure increasing heterogeneously within the domain at timesteps t_1 and t_2 , following grain boundaries and according to equations discussed above. The lookup tables used for ρ_s , ρ_f and C_s^{im} are the same as in the 1D-model for the dolerite.

Densification in the Model

In the model, porosity increases due to densification of the solid with simultaneous incorporation of water into the solid (eq. XIV), both as a result of increasing fluid pressure. Densification occurs only in relation to the already formed amphibolite at the very tip of the reaction front, while initial density of the protolith is not considered in the model because the tip of the front is assumed to always be completely hydrated.

Outlook

Expanding the numerical modes presented here could take multiple paths, depending on the questions that are to be answered.

Including solid deformation and the measured properties of the protoliths may give more insight into the mechanisms governing the volume generating reaction observed in the dolerite. Applying the calculated density of the dolerite as background density ρ_0 in equation XIV would result in clogging

unless initial porosity φ_0 is set high enough to be able to accommodate the resulting volume increase (about 7%). Expansion of the solid cannot happen if the current assumptions, which include a non-deforming solid, are applied. A solution for this could be an approach similar to that of Malvoisin et al. (2021), allowing solid deformation by reaction induced swelling of the rock.

The chemistry of the system could be expanded, for example by including dissolved components in the fluid such as NaCl or aqueous silica, to check if open system behavior, i.e., parts of the rock dissolving and leaving the system with the fluid, could be a reason for the texture-preserving reaction with volume expansion. Considering kinetic factors of the reaction may help to explain how the reaction front moves forward before reaction is complete, in addition to the demonstrated effect of spatial dimensions and averaging.

Conclusion

The herein described samples from the Hustad Igneous Complex in Norway present examples of incomplete lower crustal amphibolitization during late Caledonian exhumation and extension. The developed numerical models reproduce the observed difference in reaction front propagation depth between two different rock types exposed to the same conditions.

The gradient from unaffected protolith through partial and up to full transformation is especially well preserved along fractures in the Proterozoic dolerite dike that cuts through the entire Hustad Igneous Complex. Proceeding through grain boundary assisted flow and slower complete replacement of individual grains by dissolution precipitation reactions, the amphibolitization reaches up to 10 – 15 cm into the rock, normal to fractures which serve as fluid channels and are later filled with quartz-rich pegmatites. The overall reaction in the rock is 40% Ca-poor plagioclase + 20% garnet + 20% clinopyroxene \rightarrow 43% Ca-rich plagioclase + 39% amphibole \pm 3% quartz, both assemblages accompanied by biotite and oxides. Equilibrium thermodynamic calculations predict a pressure-temperature range of 650 – 730°C and 0.4 – 0.6 GPa for the formation of the amphibolite.

The massive pyroxenite body cut by the dike is also partially transformed to amphibolite along the same fractures. It consists of at least 30 vol% amphibole everywhere on the sample, but abundance increases up to 55 vol% at the fracture. This observation and the partially different composition of amphibole around the fracture, combined with local garnet zonation and phase diagrams, point to earlier pervasive amphibolitization and limited (6 – 8 cm), partial transformation by the event that amphibolitized the dolerite. The transformation did not reach full equilibrium anywhere in the pyroxenite, with residual pyroxenes still present directly at the fracture. These differences are ascribed to the mineralogy of the samples: Pervasive plagioclase recrystallization accelerates reactive fluid flow in the dolerite, and matrix-forming, pre-existing amphibole slows it down in the pyroxenite. Further insight is gained from numerical models:

One-dimensional reactive fluid flow models show a propagating reaction front in both rocks, driven by a fluid pressure gradient. The front propagates faster in the model with dolerite composition due to a steeper density and resulting porosity gradient over the same pressure range. This results in more progress over the same time, consistent with observations.

In the models, the front is very sharp, while a gradual transition is indicated in 1D-averages of the real samples. Readjusting the model to two spatial dimensions and adding a difference in background porosity between grains and boundaries results in an average gradient of reactional progress. Here,

fluid flow is faster along grain boundaries than into grains, recreating the mixture of channelized flow along grain boundaries and pervasive replacement within grains observed in the samples.

The amphibolite halos are most likely a record of retrograde metamorphism during exhumation in the context of the Caledonian orogeny (Hacker et al. 2010). They present evidence that even in an enclave of low strain embedded into highly sheared and metamorphosed gneisses, fluid flow occurs and induces partial equilibration of the system. The samples also serve as further evidence that fluids are capable of infiltrating effectively impermeable rocks at depth while being incorporated into them. In addition, they show the transient stages of this process and reveal some of the reaction mechanisms that govern the evolution of mafic rocks in the lower crust, pointing to plagioclase as an important player in metasomatism of mafic crustal rocks.

Acknowledgements

I would like to thank my supervisors, Hans Vrijmoed and Timm John, for taking me to Norway and giving me the chance to collect and work on my own samples. Thank you for training and challenging me over the course of this thesis, and for all the ideas and discussions. I would also like to thank Christiane Behr for preparing the thin sections, and Moritz Liesegang for preparing me to work the microprobe alone. A very special thanks goes to the Geocafe, for 6 years of great company, conversations, and kicker matches!

References

- Ague, J.J., and Axler, J.A. (2016) Interface coupled dissolution-precipitation in garnet from subducted granulites and ultrahigh-pressure rocks revealed by phosphorous, sodium, and titanium zonation. *American Mineralogist*, 101 (7), 1696–1699, doi: 10.2138/am-2016-5707.
- Apted, M.J., and Liou, J.G. (1983) Phase relations among greenschist, epidote-amphibolite, and amphibolite in a basaltic system. *American Journal of Science*, 283 (A), 328–354.
- Audétat, A., and Edmonds, M. (2020) Magmatic-Hydrothermal Fluids. *Elements*, 16 (6), 401–406, doi: 10.2138/gselements.16.6.401.
- Austrheim, H. (1987) Eclogitization of lower crustal granulites by fluid migration through shear zones. *Earth and Planetary Science Letters*, 81 (2-3), 221–232, doi: 10.1016/0012-821X(87)90158-0.
- Austrheim, H., Corfu, F., Bryhni, I., and Andersen, T.B. (2003) The Proterozoic Hustad igneous complex: a low strain enclave with a key to the history of the Western Gneiss Region of Norway. *Precambrian Research*, 120 (1-2), 149–175, doi: 10.1016/s0301-9268(02)00167-5.
- Bach, W., and Früh-Green, G.L. (2010) Alteration of the Oceanic Lithosphere and Implications for Seafloor Processes. *Elements*, 6 (3), 173–178, doi: 10.2113/gselements.6.3.173.
- Beinlich, A., John, T., Vrijmoed, J.C., Tominaga, M., Magna, T., and Podladchikov, Y.Y. (2020) Instantaneous rock transformations in the deep crust driven by reactive fluid flow. *Nature Geoscience*, 13 (4), 307–311, doi: 10.1038/s41561-020-0554-9.
- Berckhemer, H. (1968) Topographie des "Ivrea-Körpers" abgeleitet aus seismischen und gravimetrischen Daten. *Schweizerische mineralogische und petrographische Mitteilungen*, 48 (1), 235–246, doi: 10.5169/SEALS-37767.
- Bessat, A., Duretz, T., Hetényi, G., Pilet, S., and Schmalholz, S.M. (2020) Stress and deformation mechanisms at a subduction zone: insights from 2-D thermomechanical numerical modelling. *Geophysical Journal International*, 221 (3), 1605–1625, doi: 10.1093/gji/ggaa092.
- Boutonnet, E., Leloup, P.H., Sassier, C., Gardien, V., and Ricard, Y. (2013) Ductile strain rate measurements document long-term strain localization in the continental crust. *Geology*, 41 (8), 819–822, doi: 10.1130/G33723.1.

- Bucher, K. (2023) *Petrogenesis of Metamorphic Rocks*, 9th ed., 467 p. Springer International Publishing; Imprint Springer, Cham, doi: 10.1007/978-3-031-12595-9.
- Candiotti, L.G., Duretz, T., and Schmalholz, S.M. (2022) Horizontal Force Required for Subduction Initiation at Passive Margins With Constraints From Slab Detachment. *Frontiers in Earth Science*, 10, doi: 10.3389/feart.2022.785418.
- Cocks, L., and Torsvik, T.H. (2002) Earth geography from 500 to 400 million years ago: a faunal and palaeomagnetic review. *Journal of the Geological Society*, 159 (6), 631–644, doi: 10.1144/0016-764901-118.
- Corfu, F., Andersen, T.B., and Gasser, D. (2014) The Scandinavian Caledonides: main features, conceptual advances and critical questions. Geological Society, London, Special Publications, 390 (1), 9–43, doi: 10.1144/SP390.25.
- Duretz, T., Borst, R., and Yamato, P. (2021) Modeling Lithospheric Deformation Using a Compressible Visco-Elasto-Viscoplastic Rheology and the Effective Viscosity Approach. *Geochemistry, Geophysics, Geosystems*, 22 (8), doi: 10.1029/2021GC009675.
- England, P.C., and Thompson, A.B. (1984) Pressure--Temperature--Time Paths of Regional Metamorphism I. Heat Transfer during the Evolution of Regions of Thickened Continental Crust. *Journal of Petrology*, 25 (4), 894–928, doi: 10.1093/petrology/25.4.894.
- Eskola, P. (1915) On the relations between the chemical and mineralogical composition in the metamorphic rocks of the Orijarvi region. *Bulletin de la Commission geologique de Finlande*, 44, 109–145.
- Evans, K.A., and Tomkins, A.G. (2020) Metamorphic Fluids in Orogenic Settings. *Elements*, 16 (6), 381–387, doi: 10.2138/gselements.16.6.381.
- Evans, B.W., Hattori, K., and Baronnet, A. (2013) Serpentinite: What, Why, Where? *Elements*, 9 (2), 99–106, doi: 10.2113/gselements.9.2.99.
- Finnie, I. (1995) Some reflections on the past and future of erosion. *Wear*, 186–187, 1–10, doi: 10.1016/0043-1648(95)07188-1.
- Griera, A., Bons, P.D., Jessell, M.W., Lebensohn, R.A., Evans, L., and Gomez-Rivas, E. (2011) Strain localization and porphyroclast rotation. *Geology*, 39 (3), 275–278, doi: 10.1130/G31549.1.
- Hacker, B.R., Andersen, T.B., Johnston, S., Kylander-Clark, A.R., Peterman, E.M., Walsh, E.O., and Young, D. (2010) High-temperature deformation during continental-margin subduction & exhumation: The ultrahigh-pressure Western Gneiss Region of Norway. *Tectonophysics*, 480 (1–4), 149–171, doi: 10.1016/j.tecto.2009.08.012.
- Hacker, B.R., Kelemen, P.B., and Behn, M.D. (2015) Continental Lower Crust. *Annual Review of Earth and Planetary Sciences*, 43 (1), 167–205, doi: 10.1146/annurev-earth-050212-124117.
- Heeb, J., Healy, D., Timms, N.E., and Gomez-Rivas, E. (2023) Rapid hydration and weakening of anhydrite under stress: Implications for natural hydration in the Earth's crust and mantle, doi: 10.5194/egusphere-2023-161.
- Hernes, I. (1955) Eclogite-amphibolite on the Molde peninsula, Southern Norway. *Norsk Geologisk Tidsskrift*, 33, 163–184.
- Holland, T., and Powell, R. (2011) An improved and extended internally consistent thermodynamic dataset for phases of petrological interest, involving a new equation of state for solids. *Journal of Metamorphic Geology*, 29 (3), 333–383, doi: 10.1111/j.1525-1314.2010.00923.x.
- Huber, K., Vrijmoed, J.C., and John, T. (2022) Formation of Olivine Veins by Reactive Fluid Flow in a Dehydrating Serpentinite. *Geochemistry, Geophysics, Geosystems*, 23 (6), doi: 10.1029/2021GC010267.
- Jonas, L., John, T., King, H.E., Geisler, T., and Putnis, A. (2014) The role of grain boundaries and transient porosity in rocks as fluid pathways for reaction front propagation. *Earth and Planetary Science Letters*, 386, 64–74, doi: 10.1016/j.epsl.2013.10.050.

- Kaatz, L., Zertani, S., Moulas, E., John, T., Labrousse, L., Schmalholz, S.M., and Andersen, T.B. (2021) Widening of Hydrous Shear Zones During Incipient Eclogitization of Metastable Dry and Rigid Lower Crust—Holsnøy, Western Norway. *Tectonics*, 40 (3), doi: 10.1029/2020TC006572.
- Kaatz, L., Reynes, J., Hermann, J., and John, T. (2022) How fluid infiltrates dry crustal rocks during progressive eclogitization and shear zone formation: insights from H₂O contents in nominally anhydrous minerals. *Contributions to Mineralogy and Petrology*, 177 (7), doi: 10.1007/s00410-022-01938-1.
- Kerrick, D.M., and Connolly, J.A. (2001) Metamorphic devolatilization of subducted marine sediments and the transport of volatiles into the Earth's mantle. *Nature*, 411 (6835), 293–296, doi: 10.1038/35077056.
- Kiss, D., Moulas, E., Kaus, B.J.P., and Spang, A. (2023) Decompression and Fracturing Caused by Magmatically Induced Thermal Stresses. *Journal of Geophysical Research: Solid Earth*, 128 (3), doi: 10.1029/2022JB025341.
- Kohn, M.J., and Spear, F. (2000) Retrograde net transfer reaction insurance for pressure-temperature estimates. *Geology*, 28 (12), 1127, doi: 10.1130/0091-7613(2000)28<1127:RNTRIF>2.0.CO;2.
- Leake, B.E., Woolley, A.R., Arps, C.E.S., Birch, W.D., Gilbert, M.C., Grice, J.D., Hawthorne, F.C., Kato, A., Kisch, H.J., Krivovichev, V.G., Linthout, K., Jo Laird, Mandarino, J.A., Maresch, W.V., Nickel, E.H., Rock, N.M.S., Schumacher, J.C., Smith, D.C., Stephenson, N.C.N., Ungaretti, L., Whittaker, E.J.W., and Youzhi, G. (1997) Nomenclature of amphiboles; report of the subcommittee on amphiboles of the International Mineralogical Association, Commission on New Minerals and Mineral Names. *The Canadian Mineralogist*, 35 (1), 219–246.
- Li, J.-L., Schwarzenbach, E.M., John, T., Ague, J.J., Huang, F., Gao, J., Klemd, R., Whitehouse, M.J., and Wang, X.-S. (2020) Uncovering and quantifying the subduction zone sulfur cycle from the slab perspective. *Nature Communications*, 11 (1), 514, doi: 10.1038/s41467-019-14110-4.
- Locock, A.J. (2008) An Excel spreadsheet to recast analyses of garnet into end-member components, and a synopsis of the crystal chemistry of natural silicate garnets. *Computers & Geosciences*, 34 (12), 1769–1780, doi: 10.1016/j.cageo.2007.12.013.
- Maher, K. (2010) The dependence of chemical weathering rates on fluid residence time. *Earth and Planetary Science Letters*, 294 (1-2), 101–110, doi: 10.1016/j.epsl.2010.03.010.
- Malvoisin, B., Podladchikov, Y.Y., and Vrijmoed, J.C. (2015) Coupling changes in densities and porosity to fluid pressure variations in reactive porous fluid flow: Local thermodynamic equilibrium. *Geochemistry, Geophysics, Geosystems*, 16 (12), 4362–4387, doi: 10.1002/2015GC006019.
- Malvoisin, B., Podladchikov, Y.Y., and Myasnikov, A.V. (2021) Achieving complete reaction while the solid volume increases: A numerical model applied to serpentinisation. *Earth and Planetary Science Letters*, 563, 116859, doi: 10.1016/j.epsl.2021.116859.
- Manning, C. (2004) The chemistry of subduction-zone fluids. *Earth and Planetary Science Letters*, 223 (1-2), 1–16, doi: 10.1016/j.epsl.2004.04.030.
- Manning, C.E., and Frezzotti, M.L. (2020) Subduction-Zone Fluids. *Elements*, 16 (6), 395–400, doi: 10.2138/gselements.16.6.395.
- Marti, S., Stünitz, H., Heilbronner, R., Plümper, O., and Kilian, R. (2018) Syn-kinematic hydration reactions, dissolution-precipitation creep and grain boundary sliding in experimentally deformed plagioclase-pyroxene mixtures, doi: 10.5194/se-2018-39.
- Maruyama, S., Suzuki, K., and Liou, J.G. (1983) Greenschist-Amphibolite Transition Equilibria at Low Pressures. *Journal of Petrology*, 24 (4), 583–604, doi: 10.1093/petrology/24.4.583.
- Miyashiro, A. (1973) *Metamorphism and Metamorphic Belts* Springer Netherlands, Dordrecht, doi: 10.1007/978-94-011-6836-6.

- Park, J.-W., Campbell, I.H., Chiaradia, M., Hao, H., and Lee, C.-T. (2021) Crustal magmatic controls on the formation of porphyry copper deposits. *Nature Reviews Earth & Environment*, 2 (8), 542–557, doi: 10.1038/s43017-021-00182-8.
- Plümpner, O., Røyne, A., Magrasó, A., and Jamtveit, B. (2012) The interface-scale mechanism of reaction-induced fracturing during serpentinization. *Geology*, 40 (12), 1103–1106, doi: 10.1130/G33390.1.
- Plümpner, O., John, T., Podladchikov, Y.Y., Vrijmoed, J.C., and Scambelluri, M. (2017a) Fluid escape from subduction zones controlled by channel-forming reactive porosity. *Nature Geoscience*, 10 (2), 150–156, doi: 10.1038/ngeo2865.
- Plümpner, O., Botan, A., Los, C., Liu, Y., Malthé-Sørensen, A., and Jamtveit, B. (2017b) Fluid-driven metamorphism of the continental crust governed by nanoscale fluid flow. *Nature Geoscience*, 10 (9), 685–690, doi: 10.1038/ngeo3009.
- Poh, J., Yamato, P., Duretz, T., Gapais, D., and Ledru, P. (2020) Precambrian deformation belts in compressive tectonic regimes: A numerical perspective. *Tectonophysics*, 777, 228350, doi: 10.1016/j.tecto.2020.228350.
- Pollack, H.N. (1986) Cratonization and thermal evolution of the mantle. *Earth and Planetary Science Letters*, 80 (1-2), 175–182, doi: 10.1016/0012-821X(86)90031-2.
- Putnis, A., and Austrheim, H. (2010) Fluid-induced processes: metasomatism and metamorphism. *Geofluids*, doi: 10.1111/j.1468-8123.2010.00285.x.
- Putnis, A., and John, T. (2010) Replacement Processes in the Earth's Crust. *Elements*, 6 (3), 159–164, doi: 10.2113/gselements.6.3.159.
- Räss, L., Duretz, T., and Podladchikov, Y.Y. (2019) Resolving hydromechanical coupling in two and three dimensions: spontaneous channelling of porous fluids owing to decompaction weakening. *Geophysical Journal International*, 218 (3), 1591–1616, doi: 10.1093/gji/ggz239.
- Reyners, M., Eberhart-Phillips, D., and Stuart, G. (2007) The role of fluids in lower-crustal earthquakes near continental rifts. *Nature*, 446 (7139), 1075–1078, doi: 10.1038/nature05743.
- Ridolfi, F., Zanetti, A., Renzulli, A., Perugini, D., Holtz, F., and Oberti, R. (2018) AMFORM, a new mass-based model for the calculation of the unit formula of amphiboles from electron microprobe analyses. *American Mineralogist*, 103 (7), 1112–1125, doi: 10.2138/am-2018-6385.
- Rudnick, R.L., and Gao, S. (2014) Composition of the Continental Crust, *Treatise on Geochemistry*, p. 1–51. Elsevier.
- Rummel, L., Kaus, B.J.P., Baumann, T.S., White, R.W., and Riel, N. (2020) Insights into the Compositional Evolution of Crustal Magmatic Systems from Coupled Petrological-Geodynamical Models. *Journal of Petrology*, 61 (2), doi: 10.1093/petrology/egaa029.
- Sammon, L.G., and McDonough, W.F. (2021) A Geochemical Review of Amphibolite, Granulite, and Eclogite Facies Lithologies: Perspectives on the Deep Continental Crust. *Journal of Geophysical Research: Solid Earth*, 126 (12), doi: 10.1029/2021JB022791.
- Schmalholz, S.M., Moulas, E., Plümpner, O., Myasnikov, A.V., and Podladchikov, Y.Y. (2020) 2D Hydro-Mechanical-Chemical Modeling of (De)hydration Reactions in Deforming Heterogeneous Rock: The Periclase-Brucite Model Reaction. *Geochemistry, Geophysics, Geosystems*, 21 (11), doi: 10.1029/2020GC009351.
- Schwarzenbach, E.M., and Steele-MacInnis, M. (2020) Fluids in Submarine Mid-Ocean Ridge Hydrothermal Settings. *Elements*, 16 (6), 389–394, doi: 10.2138/gselements.16.6.389.
- Sievert, T., Wolter, A., and Singh, N.B. (2005) Hydration of anhydrite of gypsum (CaSO₄.II) in a ball mill. *Cement and Concrete Research*, 35 (4), 623–630, doi: 10.1016/j.cemconres.2004.02.010.
- Spang, A., Burton, M., Kaus, B.J.P., and Sigmundsson, F. (2022) Quantification of Volcano Deformation Caused by Volatile Accumulation and Release. *Geophysical Research Letters*, 49 (10), doi: 10.1029/2021GL097502.

- Spear, F.S. (1982) Phase Equilibria of Amphibolites from the Post Pond Volcanics, Mt. Cube Quadrangle, Vermont. *Journal of Petrology*, 23 (3), 383–426, doi: 10.1093/petrology/23.3.383.
- Spitz, R., Bauville, A., Epard, J.-L., Kaus, B.J.P., Popov, A.A., and Schmalholz, S.M. (2020) Control of 3-D tectonic inheritance on fold-and-thrust belts: insights from 3-D numerical models and application to the Helvetic nappe system. *Solid Earth*, 11 (3), 999–1026, doi: 10.5194/se-11-999-2020.
- Steele-MacInnis, M., and Manning, C.E. (2020) Hydrothermal Properties of Geologic Fluids. *Elements*, 16 (6), 375–380, doi: 10.2138/gselements.16.6.375.
- Taetz, S., John, T., Bröcker, M., Spandler, C., and Stracke, A. (2018) Fast intraslab fluid-flow events linked to pulses of high pore fluid pressure at the subducted plate interface. *Earth and Planetary Science Letters*, 482, 33–43, doi: 10.1016/j.epsl.2017.10.044.
- Vaughan-Hammon, J.D., Candiotti, L.G., Duretz, T., and Schmalholz, S.M. (2022) Metamorphic Facies Distribution in the Western Alps Predicted by Petrological-Thermomechanical Models of Syn-Convergent Exhumation. *Geochemistry, Geophysics, Geosystems*, 23 (8), doi: 10.1029/2021GC009898.
- Vrijmoed, J.C., and Podladchikov, Y.Y. (2022) Thermolab: A Thermodynamics Laboratory for Nonlinear Transport Processes in Open Systems. *Geochemistry, Geophysics, Geosystems*, 23 (4), doi: 10.1029/2021GC010303.
- Vrijmoed, J.C., van Roermund, H.L.M., and Davies, G.R. (2006) Evidence for diamond-grade ultra-high pressure metamorphism and fluid interaction in the Svartberget Fe–Ti garnet peridotite–websterite body, Western Gneiss Region, Norway. *Mineralogy and Petrology*, 88 (1-2), 381–405, doi: 10.1007/s00710-006-0160-6.
- Wedepohl, H.K. (1995) The composition of the continental crust. *Geochimica et Cosmochimica Acta*, 59 (7), 1217–1232, doi: 10.1016/0016-7037(95)00038-2.
- Wirth, R., Kruhl, J.H., Morales, L.F.G., and Schreiber, A. (2022) Partially open grain and phase boundaries as fluid pathways in metamorphic and magmatic rocks. *Journal of Metamorphic Geology*, 40 (1), 67–85, doi: 10.1111/jmg.12610.
- Yamato, P., Duretz, T., Baisset, M., and Luisier, C. (2022) Reaction-induced volume change triggers brittle failure at eclogite facies conditions. *Earth and Planetary Science Letters*, 584, 117520, doi: 10.1016/j.epsl.2022.117520.
- Zertani, S., John, T., Brachmann, C., Vrijmoed, J.C., and Plümper, O. (2022) Reactive fluid flow guided by grain-scale equilibrium reactions during eclogitization of dry crustal rocks. *Contributions to Mineralogy and Petrology*, 177 (6), doi: 10.1007/s00410-022-01928-3.
- Zheng, Y., Chen, R., Xu, Z., and Zhang, S. (2016) The transport of water in subduction zones. *Science China Earth Sciences*, 59 (4), 651–682, doi: 10.1007/s11430-015-5258-4.

Supplementary materials

The attached disk contains a copy of this work in .pdf format and the following supplementary materials:

1. Coordinates and structural measurements of the two discussed samples.
2. Thin section scans of the samples under polarized and cross-polarized light.
3. Element and phase maps in .mat format and MATLAB codes to generate them.
4. Electron microprobe point measurements and maps including used calculation spreadsheets.
5. MATLAB code files used for thermodynamic calculations (phase diagrams and lookup tables).
6. MATLAB code files of one- and two-dimensional modeling.
7. Short video files of the one- and two-dimensional models.
8. All figures shown in this work.